DEVELOPMENT AND CHARACTERIZATION OF A DIRECT DETECTION FIBER OPTIC DISTRIBUTED ACOUSTIC SENSOR

A THESIS SUBMITTED TO

THE GRADUATE SCHOOL OF ENGINEERING AND SCIENCE

OF BILKENT UNIVERSITY

IN PARTIAL FULFILLMENT OF THE REQUIREMENTS FOR

THE DEGREE OF

MASTER OF SCIENCE

IN

ELECTRICAL AND ELECTRONICS ENGINEERING

By

Faruk Uyar

September 2018

DEVELOPMENT AND CHARACTERIZATION OF A DIRECT DETECTION FIBER OPTIC DISTRIBUTED ACOUSTIC SENSOR
By Faruk Uyar
September 2018

We certify that we have read this thesis and that in our opinion it is fully adequate, in scope and in quality, as a thesis for the degree of Master of Science.

Ekmel Özbay(Advisor)

İbrahim Tuna Özdür(Co-Advisor)

Vakur Behçet Ertürk

Sefer Bora Lişesivdin

Approved for the Graduate School of Engineering and Science:

Ezhan Karaşan
Director of the Graduate School

ABSTRACT

DEVELOPMENT AND CHARACTERIZATION OF A DIRECT DETECTION FIBER OPTIC DISTRIBUTED ACOUSTIC SENSOR

Faruk Uyar
M.S. in Electrical and Electronics Engineering
Advisor: Ekmel Özbay
September 2018

Phase-sensitive optical time domain reflectometer ($\phi-$OTDR) based distributed acoustic sensor (DAS) systems have attracted increasing attention in recent years due to their remarkable advantages in a wide range of industrial and military applications such as health monitoring and security of civil infrastructures, railways, oil and gas pipelines, borders, and so on. They measure vibrations and detect perturbations along a section of fiber. Different approaches have been adopted to realize the $\phi-$OTDR systems and process the data from these sensors.

In this thesis, a direct detection DAS based on $\phi-$OTDR architecture with long sensing range and high signal-to-noise ratio (SNR) is demonstrated. Testing and characterization of critical system components is conducted before integrating them into the system. The results of laboratory tests are presented, in which the detected traces are successively analyzed in order to localize and investigate the perturbation events along the test fibers. The field tests are demonstrated with different external events such as digging, walking, and motor vibration. Considering the random nature of Rayleigh backscattered light and fading effect encountered in these tests, a new performance metric, which is Mean SNR, is proposed for assessing and comparing the system performances. Besides, statistical characteristics of the SNR of the vibration events in different distances for both laboratory tests and field tests is experimentally measured. The photon statistics of Rayleigh backscattered signal in a $\phi-$OTDR based fiber sensor in the presence of amplified spontaneous emission noise is theoretically modeled and experimentally demonstrated, as well.

Keywords: Distributed acoustic sensor, optical time domain reflectometer, $\phi-$OTDR, Rayleigh scattering, fading, fiber optics.

ÖZET

DOĞRUDAN ALGILAMA BİR FİBER OPTİK DAĞITIK AKUSTİK SENSÖRÜN GELİŞTİRİLMESİ VE KARAKTERİZASYONU

Faruk Uyar
Elektrik Elektronik Mühendisliği, Yüksek Lisans
Tez Danışmanı: Ekmel Özbay
Eylül 2018

Faz-duyarlı optik zaman alanı reflektometresi ($\phi-$OTDR) tabanlı dağıtık akustik sensör (DAS) sistemleri, sivil altyapıları, demiryolları, petrol ve gaz boru hatları, sınır boyları vb yapıların sağlamlığının izlenmesi ve güvenliğinin sağlanması gibi pek çok askeri ve endüstriyel uygulamalarda dikkate değer avantajları nedeniyle son yıllarda artan bir ilgi çekmiştir. Bu sistemler fiberin bir bölümü boyunca titreşimleri ölçer ve ihlalleri tespit eder. $\phi-$OTDR sistemlerini gerçekleştirmek ve bu sensörlerden gelen verileri işlemek için farklı yaklaşımlar benimsenmiştir.

Bu tezde, uzun algılama menziline ve yüksek sinyal-gürültü oranına (SGO) sahip $\phi-$OTDR mimarisine dayalı bir DAS gösterilmiştir. Kritik sistem bileşenlerinin testleri ve karakterizasyonu, bunları sisteme entegre etmeden önce yapılmıştır. Test fiberi boyunca titreşim olaylarının yerinin tespit edilmesi ve incelenmesi için ardışık olarak algılanan $\phi-$OTDR izlerinin analiz edildiği laboratuvar testlerinin sonuçları sunulmuştur. Saha testleri kazma, yürüme ve motor titreşimi gibi farklı harici olaylarla gösterilmiştir. Bu testlerde karşılaşılan Rayleigh geri saçılımının rastlantısal niteliği ve sönümlenme etkisi göz önünde bulundurularak, sistem performanslarını değerlendirmek ve karşılaştırmak için yeni bir performans ölçütü olan Mean SNR önerilmiştir. Ayrıca, hem laboratuvar testleri hem de saha testleri için farklı mesafelerde titreşim olaylarının SGO'sunun istatistiksel özellikleri deneysel olarak ölçülmüştür. Bir $\phi-$OTDR tabanlı fiber sensörde, kendiliğinden yükseltilmiş emisyon gürültüsü varlığındaki foton istatistikleri, teorik olarak modellenmiş ve deneysel olarak ortaya konmuştur.

Anahtar sözcükler: Dağıtık akustik sensör, optik zaman alanı reflektrometresi (OTDR), $\phi-$OTDR, Rayleigh saçılımı, sönümlenme, fiber optik.

Acknowledgement

First and foremost, it gives me great pleasure to express my sincere gratitude and thanks to my advisor Prof. Dr. Ekmel Özbay, for his guidance, continuous support, and diligence throughout my research process. I will always hold him in high esteem for the understanding, patience and support he showed me during all times. His deep knowledge of the field, generosity and hard work will always have my respect and admiration. I would also express my great gratitude to my co-advisor Assoc. Prof. İbrahim Tuna Özdür for his instructions and suggestions during my research process. His critical thinking and profound knowledge in the field help me a lot to finish this challenge. Special thanks go to our project leader Dr. Tolga Kartaloğlu for his leadership, guidance and useful critiques of this research work. I hugely indebted to all of them for their complete support for my personal and academic works.

I would also like to express my appreciation to Prof. Dr. Vakur B. Ertürk and Prof. Dr. Sefer Bora Lişesivdin for volunteering their time to serve on my graduate committee.

I would like to thank my colleagues in Nanotam, including (but not limited to) Canberk Ünal, Bilgehan Paray, Talha Onat, Yusuf Ziya Köksal, Erman Engin, Okan Özdemir, Mustafa Erol, Mustafa Erdoğan, Can Kanbak, Mert Ergeneci, Sevda Apaydın and Büşra Gürdal for their cooperation, aid and friendship throughout my study.

My deepest gratitude goes to my family, my father İhsan, my mother Mesude, my brother Enes, and my nephew Arif for their always-present love, encouragement and support for all of these years. My appreciation also goes to my dearest friends (too many to list here) for their moral support and being always there for me. Finally, I would like to thank God for making this possible for me.

Contents

List of Figures

List of Tables

Chapter 1

Introduction

Optical fiber sensors are devices which employ fiber optic cable as the sensing element and utilize light to convey sensing information. They emerged as a novel enabling sensing technology in the 1970s following the rapid advances made in the optical fiber technology. Since that time, they have been used in a wide variety of applications for measuring and sensing various measurands.

In the optical fiber sensor technology, there are three primary types of sensors, namely single-point sensor, multi-point sensor and distributed sensor. The topologies of different kinds of sensors are shown in Figure 1.1.

Single-point sensor is the simplest topology and it measures at only one point. *Multi-point sensor*, also called quasi-distributed sensor, measures at a finite number of discrete locations. Knowing how many and where to place the sensing elements without any a priori knowledge of the spatial distribution of the fiber is a problem in multi-point sensors. Thus, multi-point sensors are generally ineffective or inefficient to use, except some specific applications. *Distributed sensor* proposes a solution to this problem and it provides a continuous spatial profile of a measurand at every point of the sensing element [1]. The entire fiber functions as multiple sensors that respond to the environmental changes. It fulfills the needs in several situations which require the sensor to detect any kind of events along the monitored area.

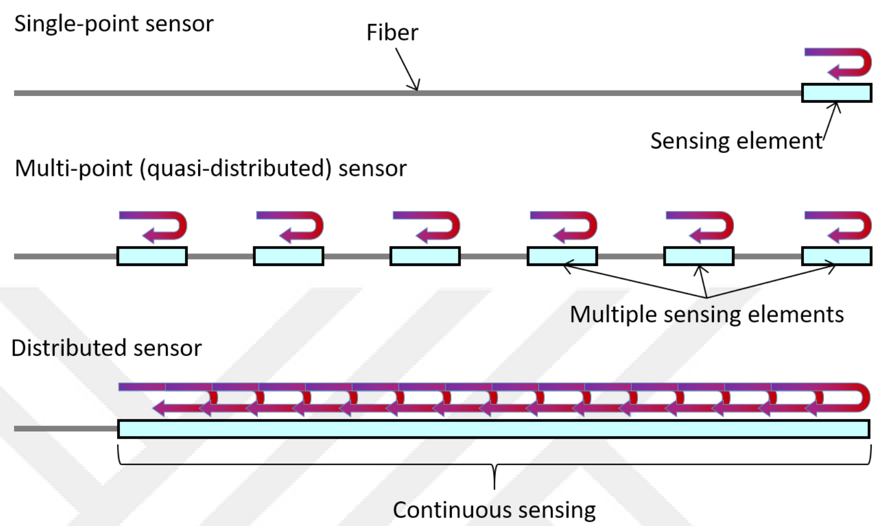

Figure 1.1: Topologies of different kinds of sensors.

Distributed optical fiber sensor (DOFS) systems are able to detect and locate the external vibration or strain signals together with the environmental changes. They carry the advantages of the general fiber sensors, including but not limited to low-loss & long range monitoring, electromagnetic interference immunity, good concealment, flexibility etc. and also offer new features such as providing the distributed vibration, temperature or strain information along the sensing fiber. They have a quick-response and highly sensitive detection for the measurands, satisfying the needs of several applications.

A major type of DOFS is descendant of optical time domain reflectometer (OTDR) which dates back to 1976 [2, 3]. OTDR technique has been used for characterizing the fiber optic link and detecting the imperfections along the long lengths of fiber based on backscatter measurements. It is a useful diagnostic tool for locating breaks, defects, losses, reflections and other anomalies in fiber optic networks, caused by the imperfections formed during the fabrication, installation or the replacement processes. An OTDR instrument launches interrogation pulses into the fiber and analyzes the returned signal in time domain. By this manner, it provides the attenuation profile of the fiber optic cable.

DOFSs which are derived from OTDR are based on the scattering of light in the optical fiber caused by various mechanisms such as Rayleigh, Brillouin and Raman scattering. The first backscattering-based distributed sensor was demonstrated in 1982 to measure temperature [4]. Following 10 years of research on DOFSs involved systems focused more on Raman and Brillouin based OTDRs [5–8]. Different types of distributed strain sensor (DSS), distributed temperature sensor (DTS), Brillouin optical time domain reflectometer (BOTDR) and so on were developed.

In the early 1990s Taylor suggested that coherent Rayleigh signal could be used for vibration sensing, [9] and first distributed vibration sensors (DVS), or distributed acoustic sensors (DAS), were demonstrated in laboratory [10, 11]. This was a breakthrough in optical sensing technology and since then several universities and companies have worked on developing DAS systems. DAS has found a widespread application in many areas, especially in health monitoring and security of large structures such as oil and gas pipelines, bridges, railways, dams and other military and civil constructions [12].

During the past 20 years, different approaches have been adopted to realize the $\phi-$OTDR system and several efforts have been made to improve the performance. These methods include coherent detection for increased sensitivity [13–15], and hybrid distributed amplification for longer range over 100 km [16, 17]. Besides, phase demodulation methods based on phase generated carrier algorithm, 3 x 3 demodulation method, frequency division multiplexing, and digital coherent detection schemes were employed to fully determine the waveform vector linearly together with increasing SNR [18–21].

One of the major problems encountered in DAS systems is fading. Regardless of the interrogation scheme, it is hard to characterize the performance of the system due to the random nature of multipoint interference of Rayleigh backscattered light and fading phenomenon [22]. Since fiber-optic DAS technologies are based on coherent interference of Rayleigh backscattered light from discrete scatterers within the pulse duration, they experience signal fading, which includes interference fading and polarization fading [22]. The former is caused by randomness of Rayleigh scattering and is one of the most important factors that limit the performance. It also raises difficulties in specifying the system performance, particularly SNR. Different techniques were implemented in order to have a reduced interference fading and relatively stable phase sensitivity [23–25]. Additionally, many studies were done to overcome the polarization fading such as adoption of polarization diversity scheme [26], interrogation with orthogonal-state of polarization pulse pair [27] and polarization-maintaining configuration [22]. Even though fading induced noise effects were remarkably mitigated in these studies, the system still suffers from fading behaviors and random fluctuations. These are even more observable in the field tests where the environmental factors such as temperature, humidity and soil hardness become relevant. Therefore, considering the randomness of the system, SNR should be statistically presented instead of a single value in order to provide a more complete and indicative figure of merit for the sensor. In the literature, limited attention was given to the statistical parameters such as mean SNR and the variance, to define the performance characteristics of the system. In a recent study, by taking into consideration the random characteristics of the system, a new figure of merit (mean SNR) was introduced to characterize and compare DAS systems [28, 29]. However, the analysis is limited to laboratory tests and coherent detection schemes; in this thesis we extend the analysis to field tests and direct detection systems.

The rest of this thesis is organized as follows: Chapter 2 presents the theoretical background of the DAS systems and the details about the concepts of Rayleigh scattering, OTDR and $\phi-$OTDR are given. In Chapter 3, the experimental configuration of our DAS system is described followed by the tests and characterizations of the critical system components. Chapter 4 provides the laboratory tests conducted with different perturbation signals at different locations along the test fibers. It also introduces a new figure of merit to assess and compare the detection performances considering the randomness of the system and fading phenomena. This chapter also provides statistical analysis of the Rayleigh backscattered signal in the presence of amplified spontaneous emission noise. Chapter 5 contains the field demonstration of our DAS system, tested with different intrusion events such as digging, walking and motor vibration. The visibility of the intrusion peaks was increased applying some signal processing algorithms. Here the performance of motor vibration detection of our system is specified in a statistical manner in which the mean SNR is determined using the histograms of the SNR. The fading characteristics of the motor vibrations at different distances is also presented. Finally, Chapter 6 concludes the thesis with a review of our work and a summary of open research topics.

Chapter 2

Theoretical Background

2.1 Optical Fibers

Optical fibers have been an enabling technology for decades in the telecommunications industry and elsewhere. It fulfills the demand of industry especially in the fields of optical communication and light transmission. Nowadays, there is a tremendous variety of industrial and laboratory applications of optical fiber technology. It has received increasing attention and become preferable solution in several areas due to its advantageous features including low loss characteristics, simple implementation, electromagnetic interference immunity and so on.

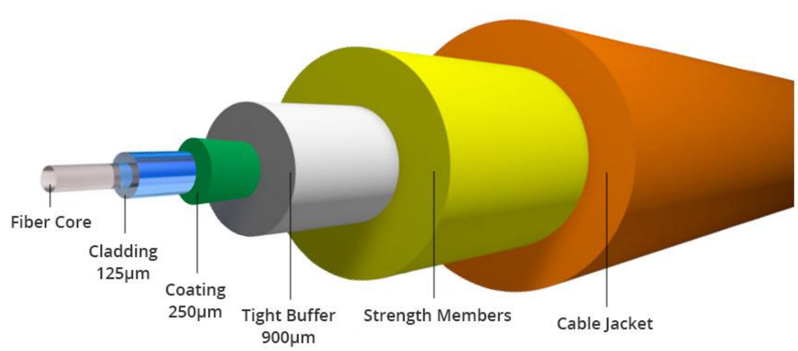

Figure 2.1: General structure of an optical fiber [30].

The general structure of an optical fiber is shown in Figure 2.1. In the simplest case, it consists of a fiber core which is the central part, and a surrounding cladding, which is the outer part. The core and the cladding have a very slight refractive index difference which leads to light trapping inside the core and waveguiding in the fibers. Such fibers are called step-index fibers due to the abrupt change of refractive index at the core-cladding interface. Cross section and refractive-index profile of a step-index fiber is shown in Figure 2.2.

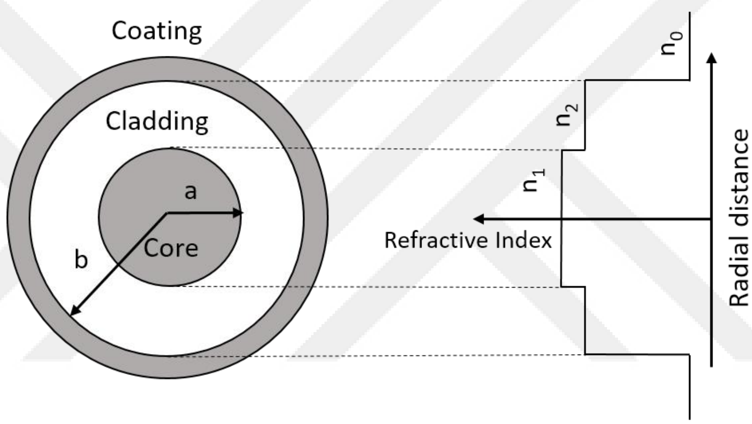

Figure 2.2: Cross section and refractive-index profile of a step-index fiber.

The coating together with outer buffers and jackets are optionally (but generally) present for the practical reasons such as structural integrity and protection of the underlying core material from the external environmental effects. The core material is generally pure silica (SiO_2) or may be modified with certain dopants like germania (GeO_2), phosphorus pentoxide (P_2O_2), or alumina (Al_2O_2) [31]. Non-silica glasses like phosphate, chalcogenide, or fluoride glasses may be the core material in the fibers, as well [31].

The light propagation in an optical fiber can be explained by the principle of total internal reflection. It is the phenomenon responsible for trapping and guiding of light in optical fibers. In this regard, it is useful to envision this mechanism with a geometrical optics approach (assuming core radius is much larger than the light wavelength) in which the light rays enter the fiber and reflect at the core-cladding interface as shown in Figure 2.3.

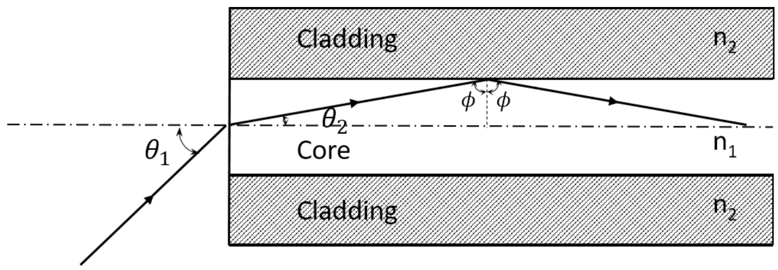

Figure 2.3: Geometrical optics approach to Total Internal Reflection in an optical fiber.

The refractions occur at the air-core and core-cladding interfaces. The relations between angles are governed by Snell's law. The final expression defining the condition for total internal reflection is given by

$$n_0 \sin\theta_1 = \sqrt{n_1^2 - n_2^2} \tag{2.1}$$

Equation 2.1 gives the expression for the numerical aperture (NA) of an optical fiber, an important parameter which describes the light-gathering ability of an optical fiber.

Introducing fractional index difference parameter, $\Delta = \frac{n_1 - n_2}{n_1}$, NA can be expressed as

$$\mathrm{NA} = \sqrt{n_1^2 - n_2^2} = n_1\sqrt{2\Delta} \tag{2.2}$$

This expression implies that Δ should be large in order to increase the capacity of the fiber to gather light. However, there is an upper limit for the increase of fractional index difference where the broadening experienced by a short pulse gets disturbing for the optical communication. This can be referred to as the modal dispersion.

Numerical aperture also determines whether the fiber is a single-mode or a multi-mode fiber. If the NA is sufficiently small, the fiber only supports the fundamental mode of the fiber, namely HE_{11}. Typical NA values for single-mode fibers are around 0.1. On the other hand, if the NA is in the range of 0.2 to 0.3 the fiber supports higher-order modes and becomes a multi-mode fiber.

Single-mode fiber is designed such that it only allows the propagation of a single mode while all other higher-order modes are cut off at the operating wavelength. The parameter that dictates the single-mode or multi-mode operation in the fiber is the normalized frequency, V, and given by

$$\mathrm{V} = \frac{2\pi a}{\lambda} = \sqrt{n_1^2 - n_2^2} = \frac{2\pi a}{\lambda}\mathrm{NA} \tag{2.3}$$

with a core radius and λ wavelength.

The cut-off number for the multi-mode operation is $\mathrm{V} = 2.405$. Thus, in the range of $0 < \mathrm{V} < 2.405$ the fiber remains single-mode. Equation 2.3 tells that single-mode fibers generally have a smaller core and lower NA than multi-mode fibers. Typical diameter sizes for core and cladding are 9 μm and 125 μm, respectively, for single-mode fiber and 50 μm/62.5 μm and 125 μm, respectively, for multi-mode fiber.

Single-mode operation can be achieved either by reduction of the core radius or reduction of the refractive index difference of the fiber, the former being more practical and common in the industry. Another alternative to achieve this is using graded-index fibers for which intermodal dispersion or multipath propagation is reduced.

Beyond the step-index and graded-index fibers there are several types of specially designed fibers which have various index profiles. Polarization maintaining fibers are first to be noted. They, by the name implies, preserve the polarization state of the input light against temperature and bending effects. They have a strong birefringence based on built-in asymmetry [31]. Plastic optical fibers made of polymer materials [32] or microstructured fibers such as photonic crystal fibers [33, 34] are other examples of some specially manufactured optical fibers, requiring specialized fabrication techniques.

There are losses due to absorption, scattering, and structural imperfections in the optical fibers. Critical loss mechanisms are explained below.

Attenuation. Attenuation is the decrease in the power of the light wave as it propagates through the fiber. It indicates the transmission loss of the optical fiber. Attenuation counts all the sources of power attenuation, including scattering, material absorption, radiation losses and waveguide imperfections.

Introducing the total attenuation constant α for the optical power, the power attenuation of a forward travelling wave along the fiber is given by the following relation:

$$P_{out} = P_{in} e^{(-\alpha L)} \tag{2.4}$$

with P_{in} the power launched at the input end of a fiber of length L, P_{out} output power at the end of the fiber of length L. The amount of optical power at any position can be calculated by this expression.

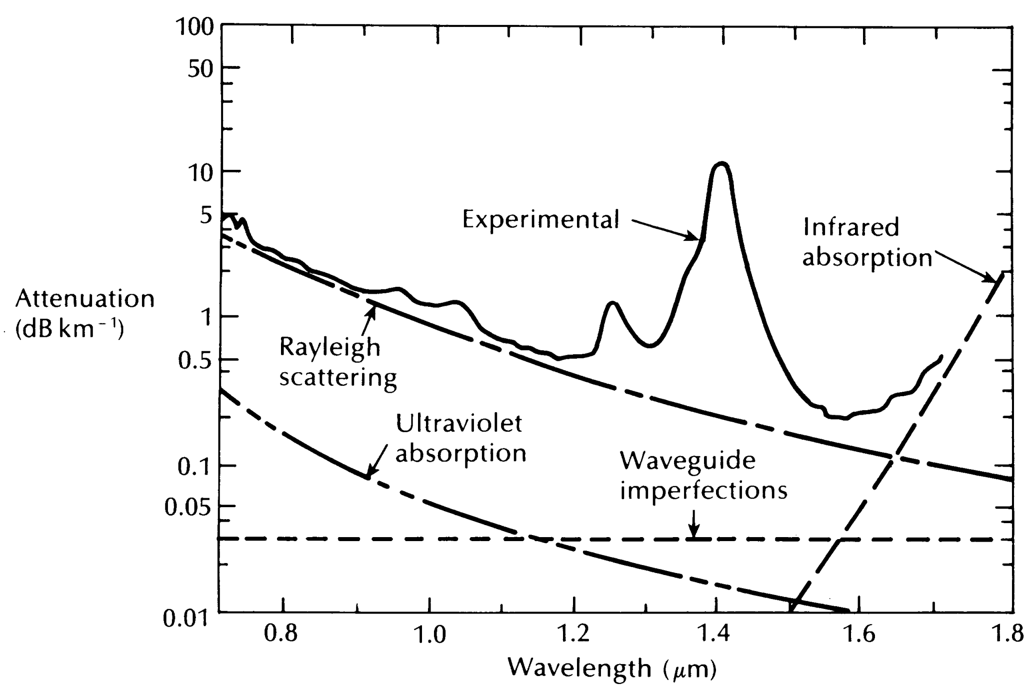

Figure 2.4: Attenuation profile of a standard optical fiber [35].

Figure 2.4 shows the attenuation profile of a standard optical fiber. Although, in the modern fibers this loss can be reduced significantly, the general pattern and limiting factors remains the same. It can be observed from Figure that Rayleigh scattering is the dominant loss mechanism and the limiting factor for the short-wavelength operation. As the wavelength increases Rayleigh scattering induced loss decreases, however then infrared absorption begins to dominate fiber loss beyond 1.6 μm. Also, there appears vibrational peaks caused by OH-ions, the largest around 1.4 μm. Therefore, this attenuation characteristics limits both the short and long-wavelength applications of optical fibers and allows limited operating windows in optical communication. The most widely operated wavelength is 1550.12 nm, accordingly, where the attenuation can be reduced below 0.2 dB/km, which makes available low-loss transmission.

Absorption. An important factor that contributes to the fiber's attenuation and becomes dominant in the infrared region is material absorption. It corresponds to the heat dissipation in the material originated from the material composition and fabrication process of the fiber [35].

Material absorption may be categorized into two types: Intrinsic and extrinsic absorption. The former describes the absorption of the fused silica itself and the latter describes the absorption caused by the impurities in the fiber.

Intrinsic absorption comprises two parts, ultraviolet absorption and infrared absorption. Ultraviolet absorption is attributed to the electrical resonances which occur and in the $\lambda < 0.4\ \mu m$ region and infrared absorption is attributed to the molecular or vibrational resonances which occur in the $\lambda > 7\ \mu m$ region. These resonances manifest themselves as the extended tails into the visible region in fused silica and place a floor of absorption loss in the attenuation profile [1, 36].

Extrinsic absorption results from different types of impurities existing in the fibers such as transition-metal ions and OH ions. Transition-metal impurities are strong absorbers in the wavelength range of 0.6-1.6 μm [36]. They can be easily purified with the state-of-the-art techniques the loss resulted from them can be alleviated in optical fibers.

The major source of extrinsic absorption is the presence of water vapor and OH ions. OH vibrational absorption at 0.6-1.3 μm range does not contribute to fiber loss much since first two spectral peaks, occurring around 0.95 μm and 1.24 μm, lie under the Rayleigh scattering with the assistance of modern loss minimization techniques. As the modern techniques are applied to minimize OH vibrational absorption, they become very small comparing to scattering loss. However, the third spectral peak which occurs near 1.39 μm causes the attenuation level rising above the scattering loss, albeit reduced to a great extent in the state-of-art good quality fibers. OH vibrational absorption becomes the dominant loss factor that creates an additional absorption peak in the attenuation profile in this wavelength range.

Scattering. Scattering causes transfer of the power carried by the forward travelling way to the reflected waves, in turn resulting in the power decrease. The redirected waves may not be captured by the core and may not contribute to the forward travelling mode. They may radiate from the fiber, which gives rise to intrinsic loss.

Two major types of linear scattering mechanisms that cause intrinsic loss are Rayleigh and Mie scattering. Rayleigh scattering arises from the molecular impurities which are far smaller than the wavelength, as will be discussed later, whereas Mie scattering arises from the large like water droplets which are comparable to the wavelength. In modern silica-based fibers, Mie-scale impurities and therefore Mie scattering is mitigated and only the Rayleigh scattering induced loss is to be considered.

Rayleigh scattering is the primary source of power loss in optical fibers, accounting for approximately 96% of attenuation in optical fibers. The remaining major loss mechanism is material absorption. If the scattering coefficient is denoted by α_s and the absorption coefficient denoted by α_a, the total attenuation coefficient α becomes

$$\alpha = \alpha_s + \alpha_a$$

The attenuation coefficients are often expressed in the unit of dB/km in practice. The scattering coefficient, α_s, equals to 0.12-0.16 dB/km and total attenuation coefficient, α, equals to 0.2 dB/km in standard optical fibers at the wavelength of 1550.12 nm. This makes the Rayleigh scattering major source of attenuation.

The light wave travelling inside the fiber exhibits exponential attenuation due to the mechanisms mentioned above. Power of the light wave can be expressed as a function of the distance z in the fiber:

$$P(z) = P_0 e^{-\alpha z} \tag{2.5}$$

where P_0 is the incident power and α is the total attenuation coefficient.

Since it is a common practice to express the attenuation coefficient in the unit of dB/km, Equation 2.5 yields,

$$P(z) = P_0 10^{\frac{-\alpha_{dB} z}{10}} \tag{2.6}$$

with $\alpha_{dB} = \frac{10}{\ln 10} \cdot \alpha = 4.34\alpha$.

Then, for example if the incident power is 20 dBm and $\alpha = 0.2$ dB/km, the power at the end of 10 km length is measured as 18 dBm excluding other losses.

2.2 Rayleigh Scattering in Optical Fibers

As previously mentioned, there are different types of scattering phenomena which are naturally observed in the fiber and DAS systems utilize the Rayleigh scattering. Rayleigh scattering is an elastic process caused by localized inhomogeneities of the refractive index of the medium through which the light wave is travelling. The other mechanisms such as Brillouin and Raman, which are inelastic, in other words the frequency of the incoming wave and the reflected waves are different, are utilized in distributed strain and temperature sensors, respectively. These mechanisms are shown in Figure 2.5.

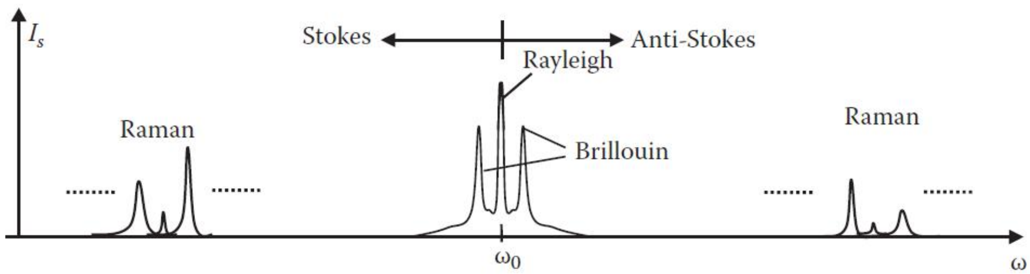

Figure 2.5: Scattering mechanisms in an optical fiber [37].

While the light wave is propagating through the fiber, it interacts with atoms and molecules inside the medium. Due to the random microscopic variations and random ordering of the molecules formed during the fabrication process of the fiber, the fiber is not perfectly homogeneous. The microscopic variation of the material structure and the density fluctuations cause the localized variations in the refractive index, which therefore gives rise to scattering. It induces attenuation, i.e. decrease of light power, and also generation of reflected waves to all directions, proportional to λ^{-4}.

This means longer wavelengths of light exhibit less scattering than shorter wavelengths. Since the scattering sites, i.e. scatterers, and the distance between them are much smaller than the light wave travelling inside the optical fiber, the reflected waves leads to coherent superposition and interference with each other.

It has been mentioned that The Rayleigh scattering coefficient is inversely proportional to the fourth power of wavelength. Its value in pure silica can be calculated as

$$\alpha_s = \frac{8\pi^3}{3\lambda^4} n_f^8 \rho^2 \beta_c k T_F \tag{2.7}$$

In this formula, λ, n_f, ρ, β_c, k, and T_F denote wavelength, refractive index, photo-elastic coefficient, isothermal compressibility, Boltzmann's constant, and fictive temperature, respectively.

We can combine all the constants in 2.7 and represent by a single constant C

such that

$$\alpha_s = \frac{C}{\lambda^4} \tag{2.8}$$

where C is in the range of $0.7 - 0.9$ $(dB/km) - \mu m^4$ [36], which means that at 1550.12 nm operating wavelength, the travelling light inside the fiber loses $2.7 - 3.6\%$ of its power for every kilometer, corresponding to 0.12-0.16 dB/km as stated earlier, due to Rayleigh scattering.

2.3 Optical Time Domain Reflectometer (OTDR)

A block diagram of a conventional Optical Time Domain Reflectometer (OTDR) is shown in Figure 2.6. In the simplest implementation of OTDR, a short probe pulse is launched into the fiber optic link. The probe pulse loses its power due to the aforementioned scattering mechanisms, including Rayleigh scattering, while propagating inside the fiber. The scattering process re-transmits the incident wave over all the directions at the same frequency. A certain small fraction of the scattered light is recaptured by the fiber core and guided back to the launching end. If there is a discontinuity, break or unexpected loss in the fiber it is detected by analyzing the reflected signal.

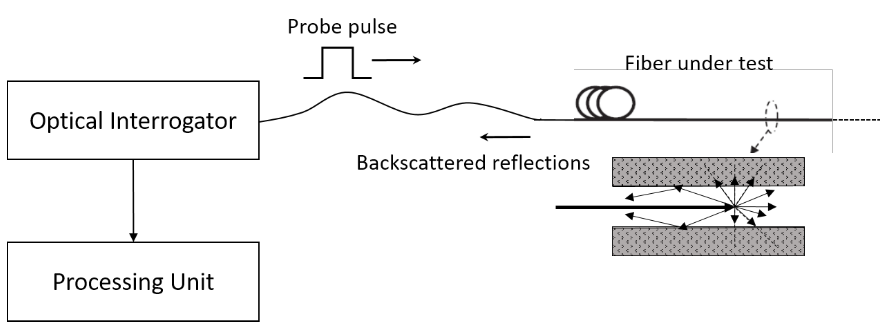

Figure 2.6: Block diagram of a conventional OTDR.

Figure 2.7 illustrates a typical OTDR fiber signature that includes the features of different types of extrinsic events such as cable joints, fusion splices, bends, connector losses and so on [38]. By interpreting the reflection features observed in OTDR measurement traces, the type and magnitude of the anomalies in the fiber can be determined.

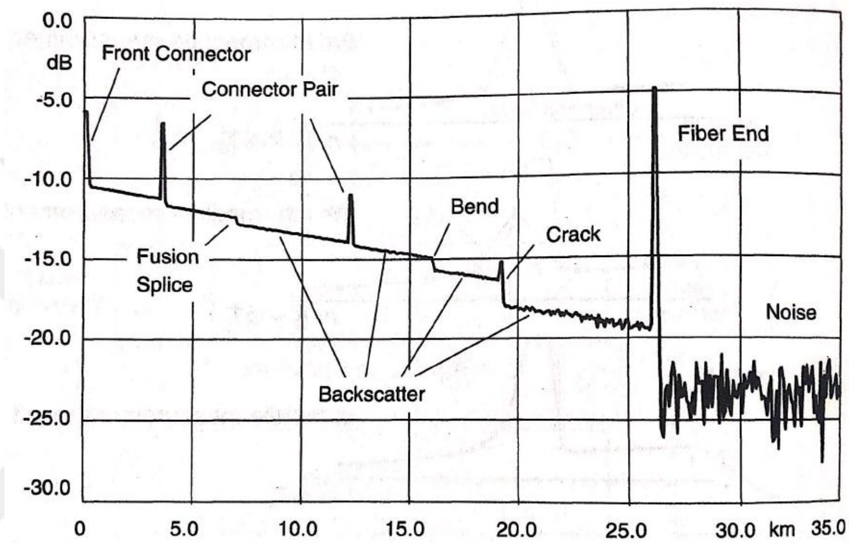

Figure 2.7: Typical OTDR fiber signature [39].

OTDR has different performance metrics, which specify the quality and capability of the instrument and measurements. These are the criteria which assess the distributed optical fiber sensors that are based on the OTDR technology, as well. Some of these parameters are explained below.

Spatial Resolution. Spatial resolution indicates the minimum resolvable distance of two consecutive reflective events that the OTDR can distinguish, which in turn defines the location accuracy of an OTDR system [12]. It depends on the spatial width of the interrogation pulses which can be expressed as:

$$W = \frac{c\Delta T}{n_f} \tag{2.9}$$

where c is the vacuum speed of light, n_f is the refractive index of the fiber, and ΔT is the pulse duration.

In literature there is a confusion with the usage of the word "pulse width". It sometimes refers to pulse width in time and sometimes refers to pulse width in space. In order to avoid this confusion, we use the word "pulse duration" to indicate the pulse width in time, denoted by ΔT and, "spatial width" to indicate the pulse width in space, denoted by W.

Taking the refractive index, i.e. n_f of the silica fiber as 1.46 and the light speed in vacuum as 2.998×10^8 m/s, the spatial width of the pulse with $\Delta T = 100$ ns is calculated as ≈ 20.53 m. Therefore the pulse travels approximately 20 m in 100 ns duration, meaning that a pulse duration of 100 ns has a spatial width of 20 m.

The fields interact with each other when they spatially overlap, corresponding to the half pulse duration. It is sometimes referred to as L_{eff} which is the interaction length between the two signals [40]. Therefore, the spatial resolution is defined by the half spatial width of the interrogation pulses such that

$$\Delta z = \frac{W}{2} = \frac{c\Delta T}{2n_f} \tag{2.10}$$

Hence it becomes ~ 10 m for a 100 ns light pulse in the example given above.

Interrogation Period and Repetition Rate. Interrogation period is the elapsed time between the adjacent traces, in other words the time waited before the subsequent pulse is injected to the sensing fiber for interrogation. The repetition rate is reverse of the interrogation period and it specifies the sampling frequency and measurement bandwidth of the system.

The maximum pulse repetition rate is limited by the length of the sensing fiber and, the interrogator must wait until one pulse completes the round-trip of the fiber, before it launches the next pulse in order to avoid backscatter signals overlapping. Therefore, minimum interrogation period must be round-trip delay of a pulse given by

$$\tau = \frac{2Ln_f}{c} \tag{2.11}$$

with L the length of the fiber, n_f the refractive index of the fiber and c the free space speed of light. For example, for a sensing fiber of 10 km, the interrogation period is required to be larger than

$$\frac{2 \times 10^4 \times 1.46}{2.998 \times 10^8} = 97.4 \approx 100 \ \mu s$$

This also yields a repetition rate of 10 kHz which limits the measurement bandwidth to 5 kHz by the Nyquist theorem. Therefore, a larger sensing range can be obtained at the expense of a smaller measurement bandwidth.

Measurement Range. The measurement range of OTDR is the maximum length of sensing fiber that can be measured. It is dependent on the combination of the incident light power to the sensing fiber and the receiver sensitivity of the instrument. It also depends on some signal processing and averaging algorithms, however, they will not be discussed here, instead some more general remarks will be noted.

The system is required to inject interrogation pulses strong enough to reach the end of the fiber under test. Plus, the receiver is required to be sensitive enough to measure the weak backscatter signals returning from the end of a long fiber. In this regard, dynamic range for an OTDR is defined as the difference between the initial signal level at the beginning of the trace and the noise level of the receiver at the end of the trace [41].

Assuming the attenuation is constant along the fiber, the backscattered power from the end of the fiber, P_{bs} can be calculated as

$$P_{bs} = \frac{F\alpha_s(\Delta T)cP_0e^{-2\alpha L}}{2n_f} \tag{2.12}$$

where α_s is the Rayleigh scattering coefficient, ΔT is the pulse duration, c is the speed of light in vacuum, P_0 is the incident peak power, α is the fiber attenuation constant, L is the length of the fiber, n_f is the refractive index, and F is the capture coefficient which varies depending on the index profile of the fiber.

The dynamic range of OTDR can be increased by either enhancing the backscattered power or by decreasing the system noise level [42]. Equation 2.12 tells that the backscattered power is proportional to $\Delta T \times P_0$. Therefore, increasing the incident light power to the sensing fiber can be achieved in two ways: increasing the peak power of the interrogation pulses or by increasing the average amount of the light power delivered, by means of launching longer pulses. The peak power from the light source is limited. Besides, the nonlinear effects such as stimulated Brillouin scattering and stimulated Raman scattering come into picture in the high peak power region which are not desired [12]. Increasing the pulse width may be an alternative to deliver larger optical energy into the fiber and enhance the dynamic range of the system, however it will reduce the spatial resolution. Therefore there is a trade-off between the dynamic range and spatial resolution at the heart of the OTDR system, which needs to be addressed and optimized depending on the application.

2.4 ϕ-OTDR

In the $\phi-$OTDR technique, the primary difference from the conventional OTDR is the usage of narrow linewidth and highly coherent light source which leads to coherence effects and multi-point interference [43,44]. It enables the instrument to be sensitive to the phase changes along the fiber originated from the changes in the fiber length, the refractive index of the fiber core, and the core diameter [45]. By this means, OTDR systems become capable of distributed intrusion monitoring and vibration sensing.

Repeated optical pulses from a highly coherent light source are injected into the sensing fiber. As the pulse propagates along the fiber, the Rayleigh backscattered light waves interfere with each other within the pulse duration. The coherent superposition of the light scattered from randomly spaced scatterers yields a $\phi-$OTDR trace exhibiting a jagged appearance as shown in Figure 2.8.

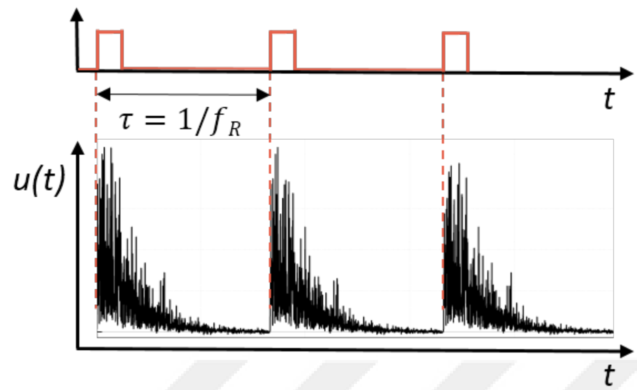

Figure 2.8: Adjacent $\phi-$OTDR traces, exhibiting jagged appearances, synchronized with interrogation pulses.

If a perturbation occurs, i.e. a mechanical wave or an acoustic wave couples to the fiber, it changes the refractive index characteristics of the fiber in that location. The refractive index change results in phase shift and change in the amount of backscattered light. The moment when the change occurs is converted to distance information using the light speed and by this means the perturbation is located on the fiber. This process is simply illustrated in Figure 2.9.

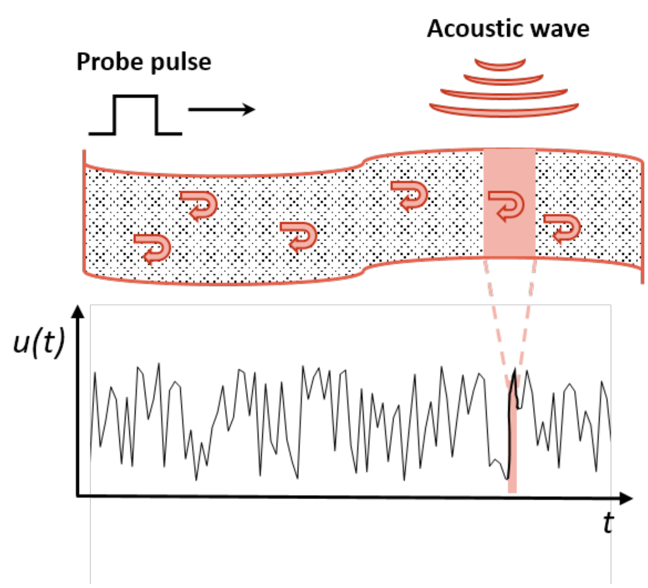

Figure 2.9: Simple illustration of $\phi-$OTDR detection process.

If the light source does not fluctuate too much and the undisturbed sections of sensing fiber are isolated from the influences of ambient, the OTDR trace will exhibit a stable appearance and only the perturbation point will be affected. The intensities of the un-perturbed channels will remain almost the same for every trace but only around the perturbation point an intensity change will appear. By taking the difference of the adjacent traces, with and without perturbation, the location and amplitude of the disturbance can be acquired.

Both the intermittent perturbations and continuous vibrations can be sensed by $\phi-$OTDR systems. In the case of continuous vibrations, $\phi-$OTDR traces will exhibit local trace-to-trace variations around the disturbance point, which will follow the vibration frequency itself. The vibration frequency can be obtained by taking the FFT of the trace data at the channels where vibration occurs.

$\phi-$OTDR systems can be modeled by the aggregate of Fabry-Perot interferometers which are distributed along the fiber and randomly located in it. Scattering and interference mechanism within a pulse can be envisioned as the reflection and interference of light from the reflectors (mirrors) of a Fabry-Perot interferometer (Figure 2.10). In the model, the mirrors at the left and right hand side have reflectance values R_1 and R_2 respectively. This represents the amplitudes of the backward-propagating waves from the leading and trailing edge of the pulse in a particular instant, or the contribution of the coherent superposition of the scatterers at the corresponding location in the fiber [40].

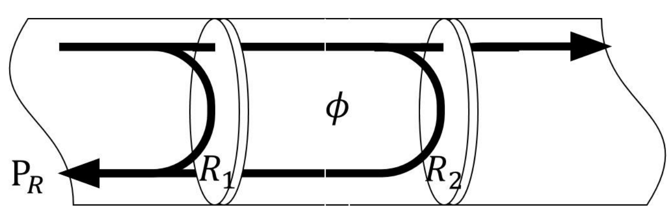

Figure 2.10: Fabry-Perot interferometer model for $\phi-$OTDR systems (Adapted from [40]).

In the Fabry-Perot model, taking into account the first reflected wave and ignoring multiple reflections from the mirrors with decreasing intensities, the reflected power, P_R, from the interferometer takes the simple form:

$$P_R = R_1 + R_2 + 2\sqrt{R_1 R_2}\cos(\phi) \tag{2.13}$$

The optical phase shift in a fiber section length L can be written as

$$\phi = \frac{2\pi n L}{\lambda} \tag{2.14}$$

When an external vibration signal is applied on the fiber section or a quantity change occurs, it will change the fiber length and/or refractive index. The corresponding phase change will become:

$$\Delta\phi = \frac{2\pi\Delta(nL)}{\lambda} \tag{2.15}$$

Fiber length or refractive index can be affected by the changes in thermodynamic quantities such as local density, entropy pressure, temperature and so on [46]. The effect of any quantity change, $\Delta\xi$, can be formulated as

$$\Delta(nL) = \left(n\frac{\partial L}{\partial \xi} + L\frac{\partial n}{\partial \xi}\right)\Delta\xi \tag{2.16}$$

As earlier noted, the sensor system can be thought of a combination of numerous reflectors which can be referred to as scatters that are sensitive to phase changes. When the launched pulses have a pulse width of W and optical frequency of ν, the backscattered wave at the input end at time t_0 will be the coherent summation of the fields backscattered from N scatterers [40, 47]:

$$E(t = t_0, z = 0) = E_0 e^{-2\alpha\bar{z}} e^{j2\pi\nu t_0} \sum_{i=1}^{N} r_i e^{j\phi_i} \tag{2.17}$$

where α is the optical fiber attenuation constant, r_i and ϕ_i are the reflectivity of the ith scatterer and relative phase of the reflected wave, respectively. They are random parameters and uniformly distributed over $[0, 1]$ and $[0, 2\pi]$, respectively.

$\bar{z}$ defines the positions of the scatterers inside the half pulse width, i.e. $W/2$, region, and expressed by $[t_0 c/n_f - W/2]/2$. Here c is the velocity of light in vacuum, and n_f is the refractive index of the fiber.

The only random parameter, which affects the statistics of the signal and contributes to fading, is $\sum_{i=1}^{N} r_i e^{j\phi_i}$ [40]. For $\phi-$OTDR systems, the backscattered signal intensity is observed, which is proportional to the square of the electric field. The intensity of the backscattered signal can be expressed as:

$$\begin{aligned} I = \left|e^{j2\pi\nu t_0}\right|^2 \left|\sum_{i=1}^{N} r_i e^{j\phi_i}\right|^2 &= \left|\sum_{i=1}^{N} r_i e^{j\phi_i}\right|^2 \\ &= \sum_{i=1}^{N} r_i^2 + 2\sum_{j=1}^{N-1}\sum_{k=j+1}^{N} r_j r_k \cos(\phi_j - \phi_k) \end{aligned} \tag{2.18}$$

where the last term describes the multi-point interference between the scattered light from numerous scatterers within the half pulse width and results in a speckle like time domain pattern of the $\phi-$OTDR trace.

If a perturbation is applied in the qth scatterer among N scatterers, which introduces a phase difference θ, then the corresponding expression for the intensity, ΔI, will be given by the intensity difference between two consecutive traces with and without perturbation:

$$\Delta I = I_{perturbed} - I_{non-perturbed} = 2\sum_{j=1}^{q-1}\sum_{k=q}^{N} r_j r_k \left[\cos(\phi_j - \phi_k) - \cos(\phi_j - \phi_k - \theta)\right] \tag{2.19}$$

This final expression models the non-linear response and interference fading behavior of the system. When $r_j r_k$ is too small or the random phases, ϕ_j and ϕ_k, of individual scatterers are in a way that they result in destructive interference, fading occurs.

2.4.1 Direct-Detection ϕ-OTDR

The direct detection scheme is the simplest configuration used in ϕ-OTDR based DAS systems, in which the signal is directly detected by the receiver. It has a low complexity and simple implementation feature, making it a good choice for the short range applications where the Rayleigh backscattering signal is strong. There are some methods to increase the range and signal-to-noise ratio (SNR) of the direct detection sensor systems, some of them being implemented in our DAS system and investigated throughout the thesis.

2.4.2 Coherent ϕ-OTDR

Coherent detection is realized by optical mixing of the backscattered signal with local oscillator (LO), i.e. the reference light. Coherent detection technique comprises balanced detection, which can greatly reduce the DC noise and significantly increase the SNR and sensitivity of the detected signal up to the shot-noise limit. This method is suitable especially for the long range applications where the Rayleigh backscattering signal is weak.

In this technique, the interference signal between the backscattered light and the LO is detected [13–15, 21]. Since the reference light is much stronger than the backscattered light in power, the intensity of the interference signal in coherent detection is much higher than the detected signal in the direct detection [42]. Thus, coherent detection becomes more advantageous for weak signal detection.

The main drawback of coherent ϕ-OTDR is its complexity and higher sensitivity to noise effects such as laser phase noise and frequency drift. Polarization mismatch between two arms is another factor causing the instability of the ϕ-OTDR traces. These factors occurring in coherent detection sensor systems need to be handled for accurate sensing and reliable performance.

Chapter 3

Experimental Set-up and Component Characterizations

3.1 Experimental Set-up

The experimental set-up for our $\phi-$OTDR based DAS system is shown in Figure 3.1. The amplified light from the narrow linewidth continuous-wave (CW) laser is passed through an acousto-optic modulator (AOM) which generates the interrogation pulses with $\sim$100 ns width and injected into the fiber via a circulator. The backscattered signal from the fiber is directed to the detection regime in which the signal flows through an erbium doped fiber amplifier (EDFA) and optical band pass filters (BPF) followed by a photodetector (PD). Optical BPFs are a combination of Add/Drop filter and Fabry-Perot (F-P) Etalon filters which were previously described in Chapter 2. They are ASE noise suppressors, which in turn providing an improved signal-to-noise ratio (SNR) of the backscattered signal. The detected signal is acquired by a data acquisition (DAQ) system and then post-processed in a PC to analyze its characteristics.

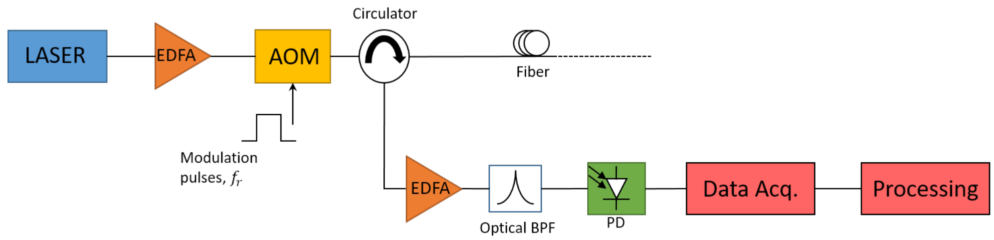

Figure 3.1: Experimental setup for DAS system. EDFA: Erbium doped fiber amplifier, AOM: Acousto-optic modulator, Optical BPF: Optical band pass filters, PD: Photodetector, Data Acq.: Data Acquisition.

3.2 Component Characterizations

3.2.1 Laser

Laser is the source of light pulses in the interrogation system. It operates at the wavelength of 1550.12 nm, the most commonly used wavelength for fiber-optic communication according to ITU standards [48], and it has a sufficiently narrow linewidth such that the interrogation pulses are coherent throughout the double length of the sensing fiber.

The important parameters of a laser, especially playing key role in DAS systems are linewidth and frequency stability / drift.

The effect of laser linewidth on fiber distributed sensing system was studied in [49] and it was shown that narrower linewidth laser results in better interference within same spatial distance. Thus, it is required for the system to have a ultra-narrow linewidth laser for higher repeatable and stable scattering spectrum [49].

The linewidth of the laser used in the experimental set-up is given as ∽100 Hz. Using the expression given below, with τ_{coh} coherence time, ν_g group velocity and $\Delta\nu$ linewidth in Lorentzian shape, the coherence length of the laser can be calculated as

$$L_{coh} = \nu_g \tau_{coh} = \frac{\nu_g}{\pi \Delta \nu} = \frac{2.05 \times 10^8}{\pi 100} \cong 652 \ km$$

which implies that the fiber length to be monitored must be below $652/2 = 326$ km in order the OTDR system to be phase-sensitive, i.e. ϕ-OTDR.

Laser frequency drift / stability is another important factor that affects the performance of a DAS system. The effect of laser frequency drift on phase-sensitivity OTDR based distributed intrusion sensor has been investigated in [50] and [51]. Zhong et al. have shown that trace-to-trace fluctuation increases with increasing laser frequency drift rate and the laser with minimum frequency drift should be chosen for better performance [51]. In this regard, before testing and characterizing the performance of our DAS system, we characterized the frequency drift / stability of four different lasers and integrated the one with the lowest frequency drift / highest stability into our fiber optic-based DAS system.

As shown in Figure 3.2, the laser under test and the reference laser are combined with a 50-50% polarization maintaining optical coupler (OC), and then the signal passes through the variable optical attenuator (VOA) and reaches to the PD. The DAQ card is employed to acquire the signal at the output of the PD.

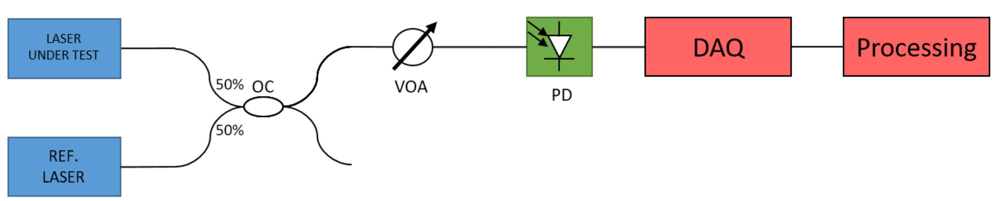

Figure 3.2: Experimental setup for frequency drift / stability characterization.

The beat note frequency drift measurements were recorded for about 20 minutes after the laser frequencies are locked to their cavity by a LabView program. The results are plotted in Figure 3.3. Besides, the extracted drift rates per minute and per 20 minutes are reported for comparison in Table 3.1. According to the results we have selected the Laser 1, which has the lowest short-term and long-term drifts, to be integrated into the system for the best performance.

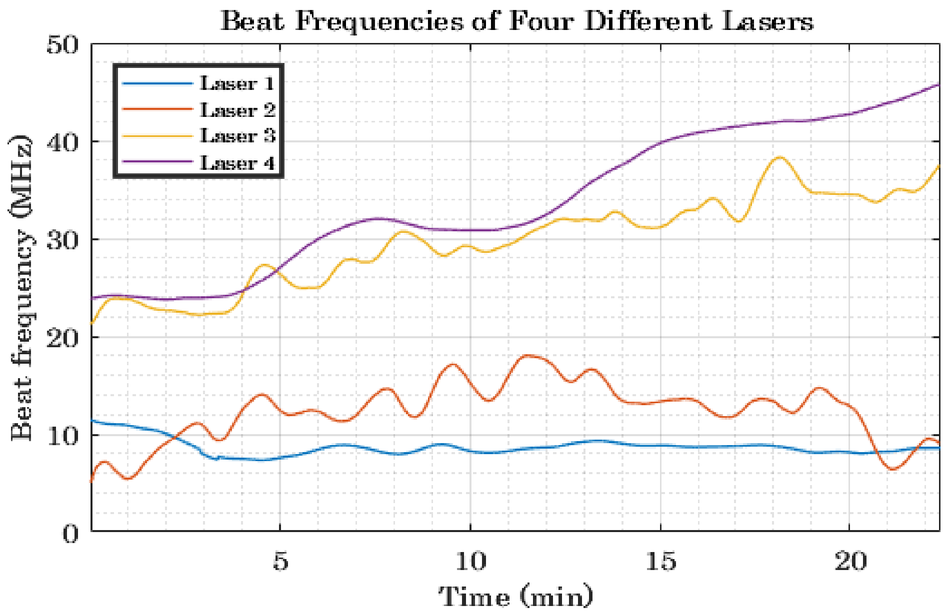

Figure 3.3: Beat note frequency drifts for 20 mins are demonstrated where beat notes are obtained by separately combining four different lasers with the reference laser.

Table 3.1: Beat note frequency drift rates per minute (short-term drift) and per 20 minutes (long-term drift)

Laser Pair	**Frequency Drift (kHz/min)**	**Frequency Drift (MHz/20 mins)**
Ref. Laser - Laser 1	127	4.11
Ref. Laser - Laser 2	179	12.98
Ref. Laser - Laser 3	729	17.10
Ref. Laser - Laser 4	972	21.96

The specifications of the selected laser to be used in the set-up are listed in Table 3.2.

Table 3.2: Laser specifications.

Linewidth (Hz)	<100
RIN level (dBc/Hz)	<-107 @peak <-140 @10MHz
Short term drift (kHz/min)	127
Long term drift (MHz/20 mins)	4.11
Max phase noise $(dB/\sqrt{rad/Hz})$	-110 @1Hz -130 @100Hz
Output power	30 mW / 14.77 dBm

3.2.2 EDFA

There are two types of optical amplifiers employed in our ϕ-OTDR based DAS system: High-power booster amplifier and High-gain preamplifier. Booster amplifier is used for maximizing the peak power of the injected pulses and preamplifier is used for amplifying the low level of backscattered intensity.

In our system two EDFAs are used for satisfying booster amplification and pre-amplification needs. As mentioned, the high power EDFA desires relatively higher levels of input and it has a high output saturation power whereas the high gain EDFA is able to amplify very low signals with high gain. Depending on the desired gain or the output power from the EDFAs, the amounts of pump currents are to be adjusted.

Gain and output characteristics of two EDFAs was studied. Figure 3.4a and 3.4b shows output power and gain vs pump current curves of the booster and preamplifier, respectively, used in the experimental set-up. They show that the booster amplifier can rise the input power up to 31 dBm and the preamplifier can provide high gain up to 55 dB.

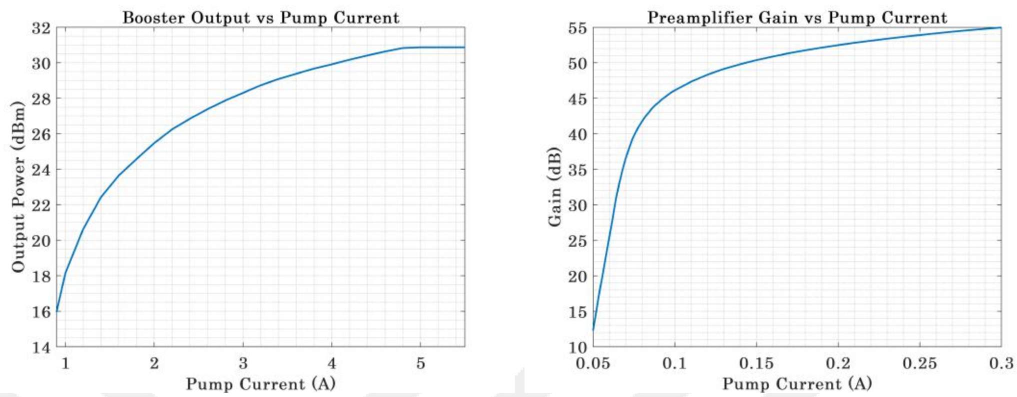

(a) (b)

Figure 3.4: a) Booster EDFA output power curve, b) Preamplifier EDFA gain curve.

3.2.3 AOM

There are different kinds of AO devices such as modulators, filters, frequency shifters, deflectors, Q-switches and so on. The working principle of AO devices is based on photo-elastic effect, in other words the interaction of light with sound in a crystalline bulk material [52]. A RF drive signal is applied to a piezo-electric transducer which generates acoustic waves inside the crystalline bulk. Similar to fiber Bragg gratings, these acoustic waves induce periodic changes in the refractive index by generating compression and rarefaction areas in the bulk material [52]. The incident light to an AO device experiences diffraction to a number of order at the output of the device. This principle is illustrated in Figure 3.5.

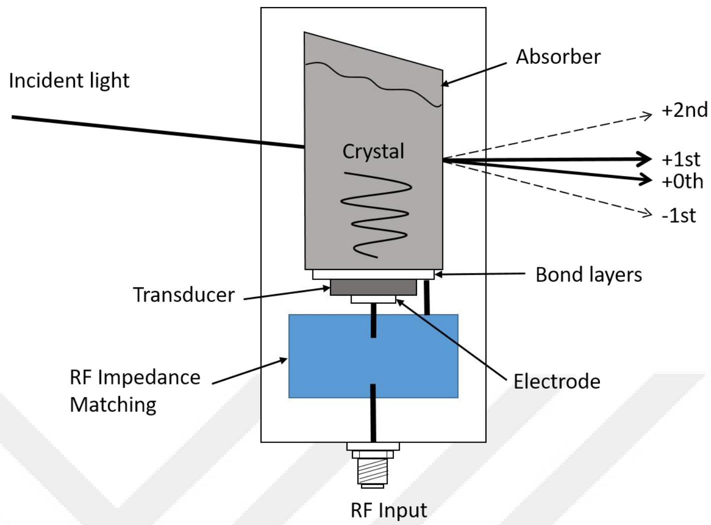

Figure 3.5: Working principle of AO devices (Adapted from [52])

In AOM's, diffraction order can be controlled by the RF input signal and the amount of light to be coupled to the optical fiber at the output can be adjusted. In this way, the light can be modulated. AOMs can be used for fast ON / OFF operations like in DAS applications.

The key parameters of an AOM are insertion loss (IL) and extinction ratio (ER). AOM devices introduce IL mainly due to the absorption in the bulk material and losses in the A/R coated surfaces. Minimizing this value is important to ensure that the optical fiber is interrogated with high-power pulses. This value can be simply calculated as

$$IL(dB) = 10log\frac{P_{out}}{P_{in}} \tag{3.1}$$

with P_{in} input power and P_{out} output power when the AOM is ON.

ER can be considered as the ON / OFF ratio of an AOM. It can be defined as the ratio of the measured optical output power when it is open, i.e. when it is driven by the RF signal, to the optical output power when it is turned off, i.e. when there is no RF signal at the RF input port and it is terminated by 50 ohm resistor. This value can be simply calculated as

$$ER(dB) = 10log\frac{P_1}{P_0} \tag{3.2}$$

with P_0 output power when the AOM is OFF and P_1 output power when the AOM is ON.

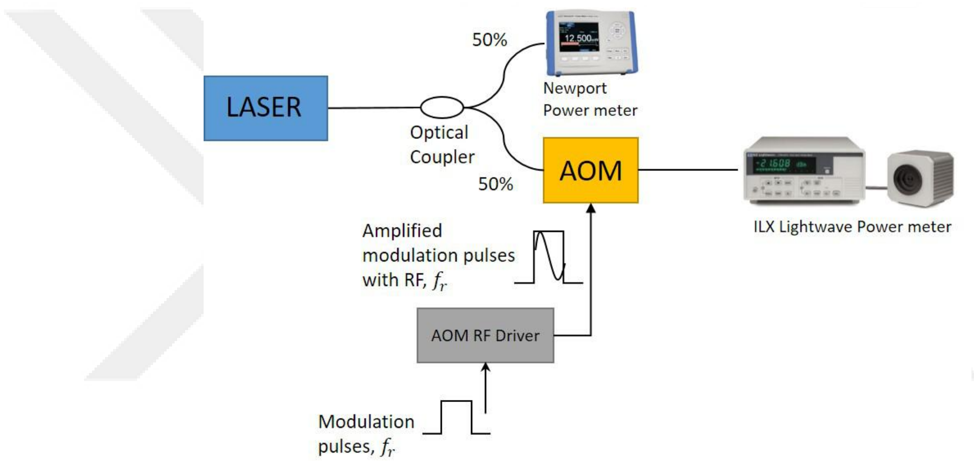

Figure 3.6: AOM characterization setup.

We characterized the AOMs in hand and measured their IL and ER values using the simple setup shown in Figure 3.6. The measurement results are listed in Table 3.3.

Table 3.3: Extinction ratio and insertion loss values of characterized AOMs

Characterized AOM	**Extinction Ratio (dB)**	**Insertion Loss (dB)**
AOM 1	58.4	4.0
AOM 2	65.8	3.6
AOM 3	70.6	3.2

3.2.3.1 The Effect of Extinction Ratio on the Rayleigh Backscattered Light

One of the limiting factors of SNR and range performance in a $\phi-$OTDR based DAS system is undesirable signal fluctuations caused by the leakage light due to the finite ER of optical pulses. Commercial AOMs employed in the experimental configuration have limited ER as characterized in the previous section. Therefore, even during the times when AOM is turned off in the interrogation system, a certain amount of CW light leaks into the fiber. Strong CW component gets reflected from the fiber, causing a background DC noise level. It also experiences coherent interference in the fiber, resulting in trace fluctuations in the signal, which can be referred to as intra-band noise [42]. We experimentally show the effect of finite ER on the Rayleigh backscattered light from a 50 km-long fiber.

The constant power of Rayleigh backscattered light from the entire fiber due to CW leakage can be calculated as

$$P_{CW} = 2\alpha_s \int_0^L P_0 e^{-2\alpha z} dz = \frac{P_0 \alpha_s \left(1 - e^{-2\alpha L}\right)}{\alpha} \tag{3.3}$$

where α_s is the Rayleigh scattering coefficient, P_0 is output power when the AOM is OFF, α is the fiber attenuation constant, and L is the length of the fiber.

Equation 3.3 and the analyses in [42], [53] indicate that the ER problem becomes more critical in the far distances since the CW component accumulates over the fiber length. Also including the coherence interference effects, the longer fiber leads to higher intra-band noise level that blurs the backscattering traces. Thus, the ER becomes the major limiting factor for long range measurement. It requires the system to have high ER interrogation pulses or reduced CW leakage.

To see the effect of AOM ER, we collected the Rayleigh backscattering light which were obtained from three AOMs with different ER values. Trace fluctuations caused by the CW interference for three AOMs are shown in Figure 3.7. It can be clearly seen that lower ER leads to more fluctuation in the traces.

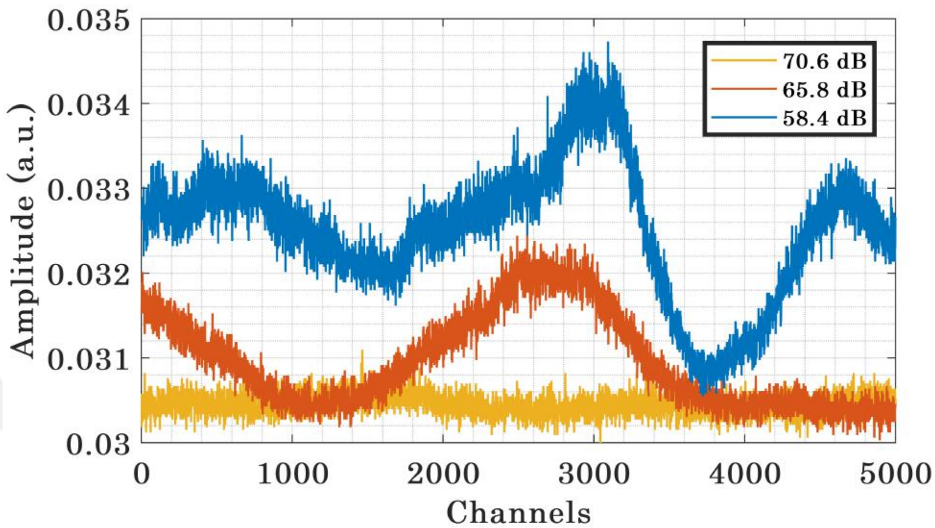

Figure 3.7: Trace fluctuations caused by the CW interference for 3 individual AOMs.

Besides, the frequency response of intra-band noise was studied and compared between the individual AOMs. The datasets were collected by a high speed DAQ card with a sampling rate of 368 MS/s. Their psd's were plotted in Figure 3.8.

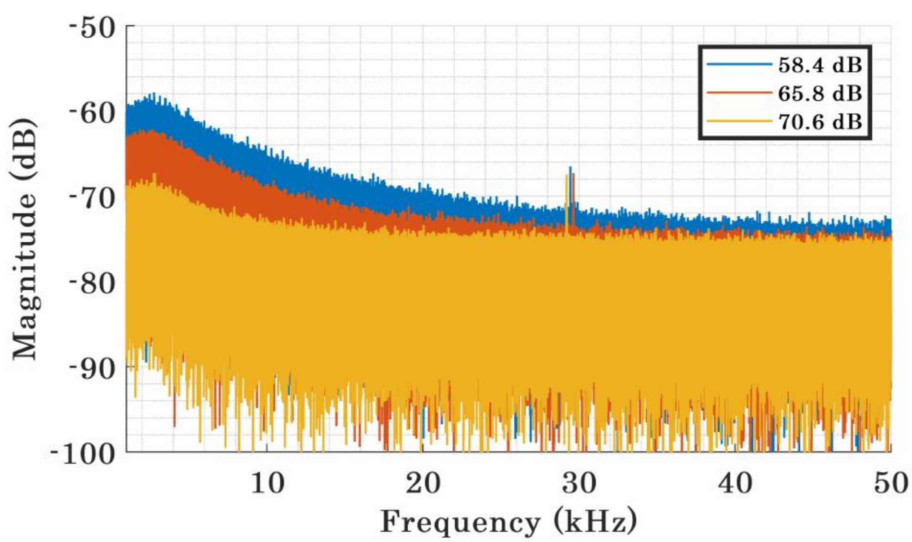

Figure 3.8: Frequency response of the backscattered light for 3 individual AOMs.

We find out that the finite ER gives rise to intra-band noise components in DC to ∽ 50 kHz interval. The intra-band noise level induced by the CW leakage goes down as the ER increases. The frequency response presented in Figure 3.8 also provides information about the laser phase noise.

3.2.4 Optical Bandpass Filter

In DAS systems optical BPFs are inserted before the photodetector. They are primarily used for the purpose of suppressing the ASE noise and thereby improving the SNR of the backscattered signal. They are used to selectively transmit a part of the optical spectrum while rejecting the other wavelengths. In our system one DWDM based Add/Drop filter with a relatively broader pass band and two Fabry-Perot (F-P) Etalon filters with relatively narrower pass bands are employed in a cascaded arrangement. The channel spacing between the passbands of the F-P Etalon filters are 25 GHz and 100 GHz, overlapping the ITU grids [48].

The filters that are employed in the system have certain pass bands. Add/Drop filter transmits wavelengths within a 0.22 nm band around 1550.12 nm and blocks longer and shorter wavelengths outside this band. As regards the F-P filters they have an FSR value with certain Finesse number determined by the reflectivity of the mirrors. Finesse number is the ratio of the FSR to the full width at half maximum (FWHM). The relations are given by

$$\mathcal{F} = \frac{\Delta\lambda}{\delta\lambda} = \frac{\pi\sqrt{\mathcal{R}}}{1-\mathcal{R}} \tag{3.4}$$

Here $\mathcal{R}$ is reflectivity of mirrors, $\Delta\lambda$ is FSR and $\delta\lambda$ is FWHM.

Therefore, for example, if a filter has 25 GHz FSR and 80% reflectivity as in the case in our system, it would have a FWHM of:

$$\delta\lambda = \frac{\Delta\lambda(1-\mathcal{R})}{\pi\sqrt{\mathcal{R}}} = \frac{25(1-0.8)}{\pi\sqrt{0.8}} = 1.786 \text{ GHz}$$

Similarly, if a filter has 100 GHz FSR and 80% reflectivity as in the case in our system, it would have a FWHM of:

$$\delta\lambda = \frac{\Delta\lambda(1-\mathcal{R})}{\pi\sqrt{\mathcal{R}}} = \frac{100(1-0.8)}{\pi\sqrt{0.8}} = 7.143 \text{ GHz}$$

The filters were firstly characterized in the Optical Spectrum Analyzer (OSA). Spectrum of a broadband source with the filters connected to its output was observed at the OSA. The FSR values of the F-P filters and the bandwidth of the Add/Drop filter were measured, accordingly. In Figures 3.9a, 3.9b, and 3.9c, transmission spectra of the Add/Drop filter, 25 GHz F-P filter and 100 GHz F-P filter are shown, respectively. In Figure 3.9d their transmission spectra were plotted overlapped for comparison.

Since the resolution of the OSA, which is 0.03 nm, corresponding to 3.75 GHz, is not sufficient for measuring the exact FWHM of the F-P filters, it was measured by optical power meter. We swept the wavelength of the narrow linewidth laser from 1520.12 nm to 1580.12 nm and recorded the output power of the filters for each nm of wavelength. We developed and used automatized LabView program for this purpose.

Figure 3.10a and 3.10b show the output power of the 25 GHz and 100 GHz filters for an input power of 14.5 dBm, respectively. The calculated FWHM values are 2.07 GHz and 7.56 GHz, respectively. Therefore, using the Equation 3.4 the reflectivity of the mirrors are calculated as 77.1% and 78.9%, respectively.

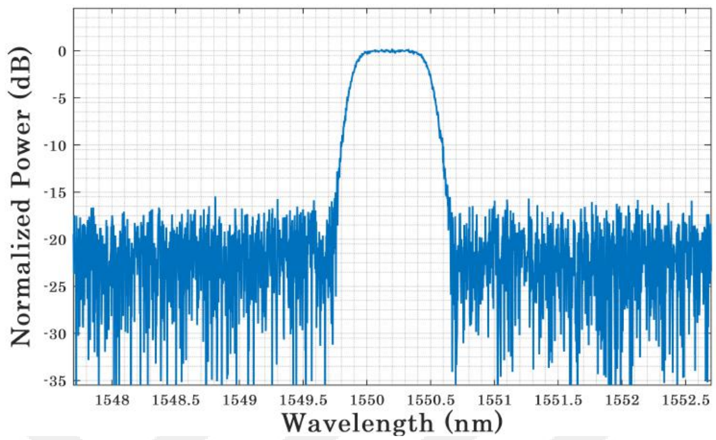

(a)

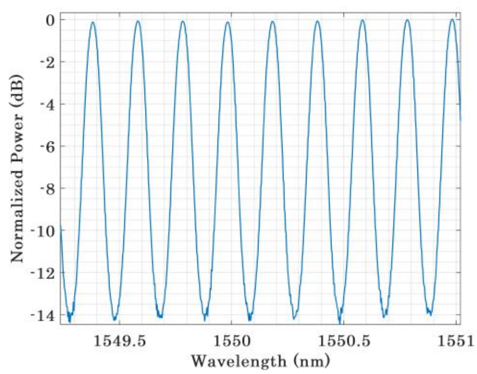

(b)

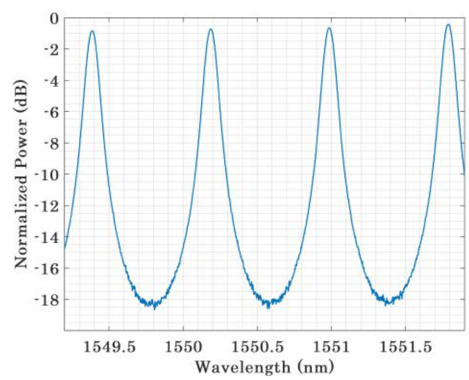

(c)

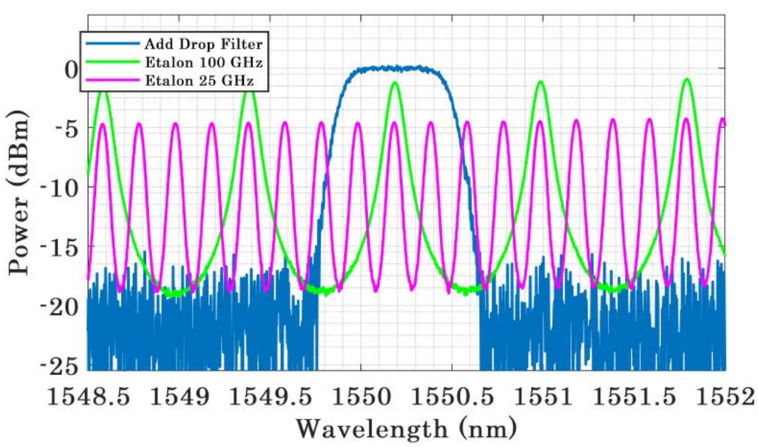

(d)

Figure 3.9: a) Add/Drop filter transmission spectrum, b) 25 GHz F-P filter transmission spectrum, c) 100 GHz F-P filter transmission spectrum, d) Transmission spectra of all of the filters overlapped.

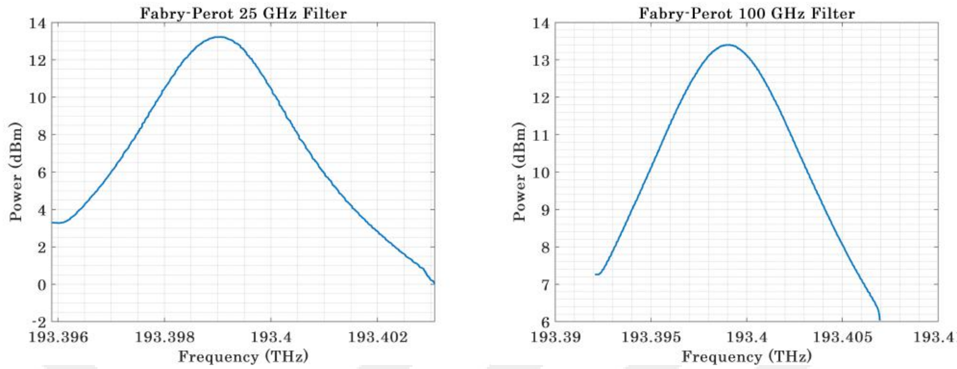

(a) (b)

Figure 3.10: Output powers for an input power of 14.5 dBm, a) F-P 25 GHz filter, b) F-P 100 GHz filter.

Finally, the amplified output of the narrow linewidth laser with the added ASE noise bands is passed through all the OBPFs and the overall optical spectrum of the filters output was displayed in OSA (Figure 3.11).

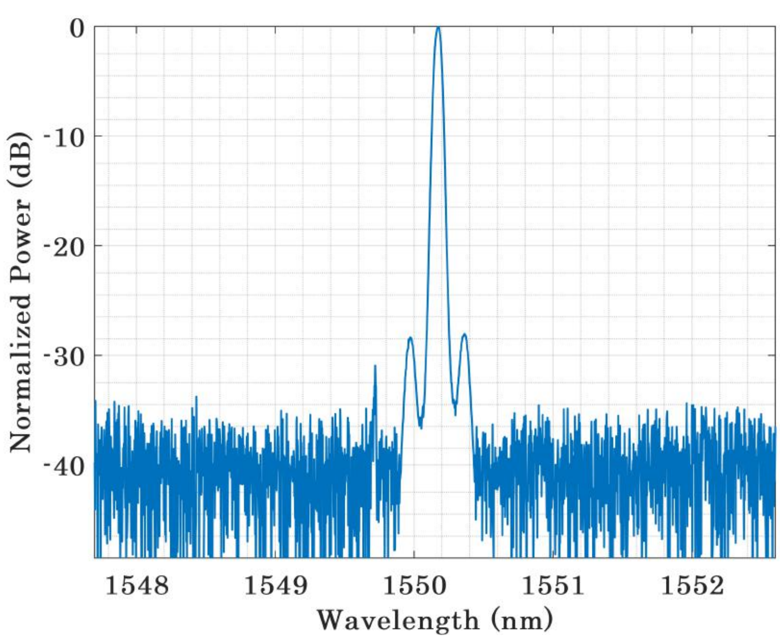

Figure 3.11: The amplified output of the narrow linewidth laser after passing through all OBPFs.

3.2.5 Photodetector

Photodetector (PD) is the component that converts light energy into electrical energy. It is based on the photoelectric effect, which is the generation of free carriers when the light illuminates a substance. PDs generally consist of a photodiode that collects the light and a trans-impedance amplifier (TIA) circuit that converts the current produced by the photodiode to a voltage.

A photodiode is a semiconductor device - often in the form of p-n or p-i-n junction- with different types and structures. When the junction region is irradiated by light, photons are absorbed and electron-hole pairs are generated in the depletion region. These pairs are collected by the electrodes by applying a reverse bias and current is produced.

A TIA is a current to voltage converter compromising an operational amplifier with feedback capacitors and resistors. It is used to amplify the low-level current output of the photodiode to a suitable voltage. The current to voltage gain is based on the feedback resistance.

In a DAS system, the light signal that returns from the fiber is collected by the photodetector unit after passing through the EDFA and optical BPFs. The filtered light signal is then converted to an electrical signal on the photodetector unit. The photodetector unit is crucial for the detection of different levels of signals and responding to rapid changes in intensity, as well as for distinguishing low-power signals from noise.

Some of the important parameters of the photodetector are noted below.

Responsivity. It is a parameter used to specify electrical output power per optical input power in photodiodes and it varies with wavelength. Responsivity of a photodiode is usually expressed in terms of amps or volts per optical power.

$$\mathcal{R}(A/W) = \frac{I_p}{P_{in}} \tag{3.5}$$

where $\mathcal{R}$ is photodiode responsivity, I_p is output current and P_{in} is input optical power.

Gain. Gain of a PD unit is calculated by multiplying the photodiode responsivity with the gain of the TIA after the photodiode.

$$G(V/W) = \mathcal{R} \times A \tag{3.6}$$

where $\mathcal{R}$ is photodiode responsivity and A is TIA gain.

Noise floor. It corresponds to the background noise level of the photodetector unit without any power incident upon it. The dark current of the photodiode together with its intrinsic resistance and the noise characteristics of the TIA are the factors that determine the output noise floor level.

We first characterized the noise characteristics of different photodiodes. They were mounted on the photodetector unit consisting of TIA and low-pass filter and then the noise levels were measured with an Audio Analyzer instrument. The measurement set-up is shown in Figure 3.12.

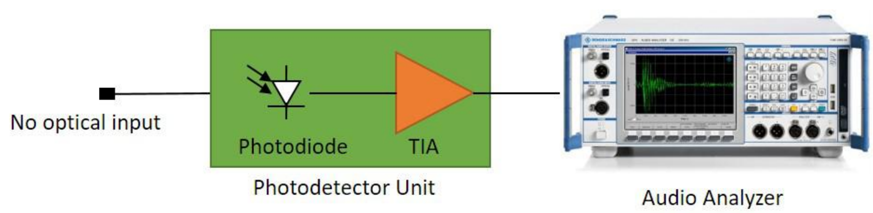

Figure 3.12: Photodetector unit noise level characterization set-up.

Figure 3.13 shows the power spectral densities after averaging of the photodetector unit with three different photodiodes mounted on it. The noise level of the Audio Analyzer instrument is also included for reference. The results show that noise floors of the PD unit with photodiode-1 and photodiode-2 are almost the same and around -142 dBm/Hz whereas the noise floor of the PD unit with photodiode-3 is higher with a value of -140 dBm/Hz. This suggests that photodiode-1 and photodiode-2 are better choices in terms of noise characteristics.

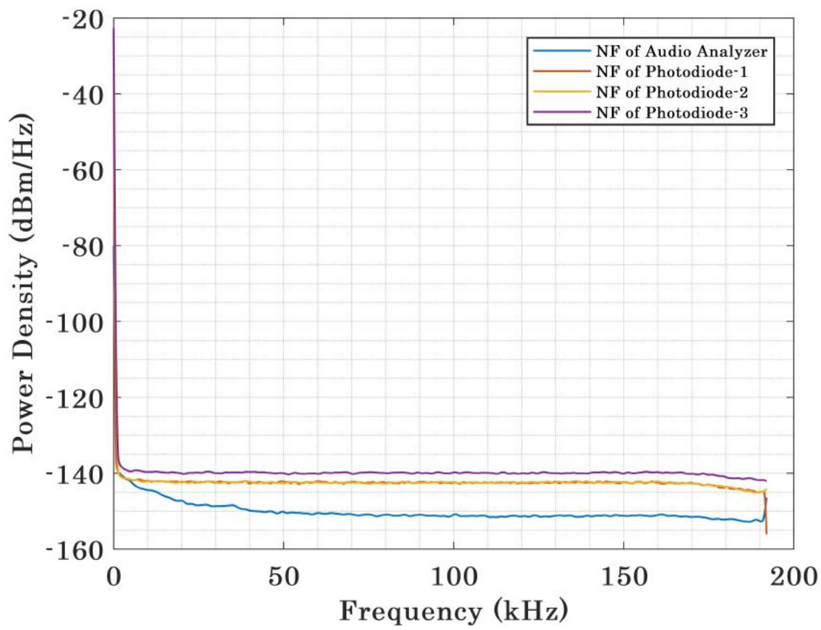

Figure 3.13: Noise spectral densities of photodetector units on which different photodiodes are mounted.

After noise characterizations, photodiode responsivity together with the gain of the photodetector unit were measured. The set-up for this measurement is shown in Figure 3.14.

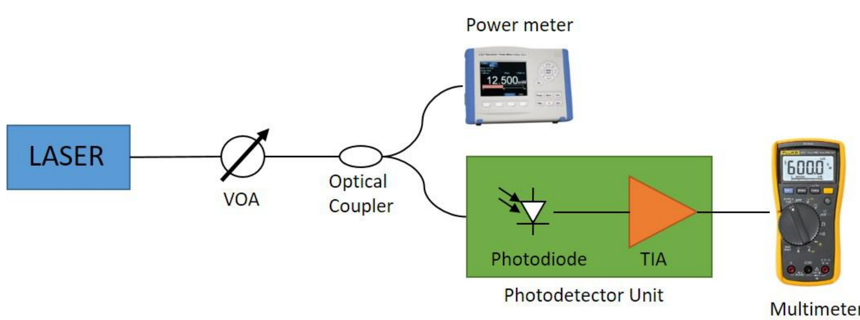

Figure 3.14: Photodetector gain / Photodiode responsivity characterization set-up.

Figure 3.15 shows the plot of measured output voltage versus optical input power for PDs with different photodiodes mounted on them. The overall gain of the PD unit is dependent on the combination of the photodiode responsivity and the gain of TIA circuit. Accordingly, for photodiode-1 and photodiode-3, the photodetector gain is calculated as 2.3×10^4 V/W whereas for photodiode-2 it is calculated as 1.9×10^4 V/W in the linear regime. This is due to the relatively smaller responsivity of photodiode-2. It can also be observed that the output of the PD saturates at high input levels above 100 μW.

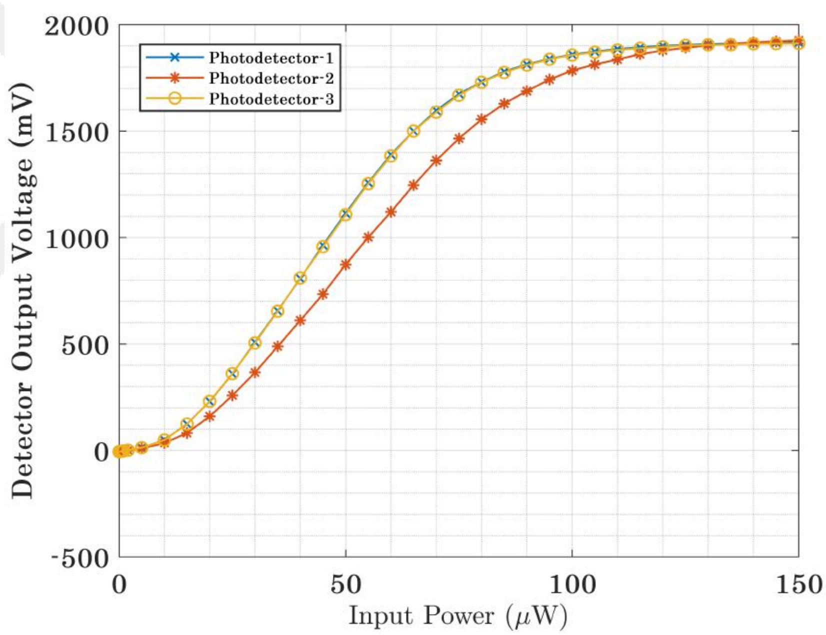

Figure 3.15: Optical input power vs output voltage curve of the photodetector units on which different photodiodes are mounted.

Chapter 4

Laboratory Tests and Statistical Analyses

4.1 PZT Vibration Tests in Laboratory

4.1.1 Test Fibers and Fiber Stretchers

After the component characterizations, the performance of the DAS system was preliminarily tested in the laboratory with the configuration shown in Figure 3.1. In the laboratory tests two different test fibers with fiber stretchers (Piezoelectric Transducer - PZT) were used. PZTs are fiber wound piezoelectric elements for simulating external vibration events. They operate on the basis of pizeoelectric effect, where the applied electric voltage produces mechanical stress or forces on piezo material. The fiber wound on the material is stretched and compressed depending on the applied voltage. This creates optical path displacement, which in turn phase shift. We use a high speed and highly linear PZT in our test set-ups. Some of the important parameters of the PZTs are listed in Table 4.1.

Table 4.1: PZT Specifcations.

Operational Wavelengths	780-1625 nm
V_π [< 5 kHz]	3.4 V
Fiber Length	12.7 m
First Resonance	@57 kHz
Linearity error [DC-5 kHz]	Drive < 30 Vp-p: < 0.5%

The first fiber under test, which is shown in Figure 4.1a, was 17 km long single-mode fiber (SMF-28). Three fiber coils of 1 km, 15 km and 1 km were connected together to obtain a 17 km test fiber. Two PZTs were placed at the positions of 1 km and 16 km to function as the vibration sources and an Arbitrary Waveform Generator (AWG) was used to drive the PZTs. The PZTs comprise ∼12m of fiber wounded which were subjected to dynamic vibration events. Similarly the second fiber under test, which is shown in Figure 4.1b, was a 41 km long SMF-28 with three fiber coils of 25 km, 15 km and 1 km connected together and two PZTs located at the positions of 25 km and 40 km for monitoring relatively larger distances.

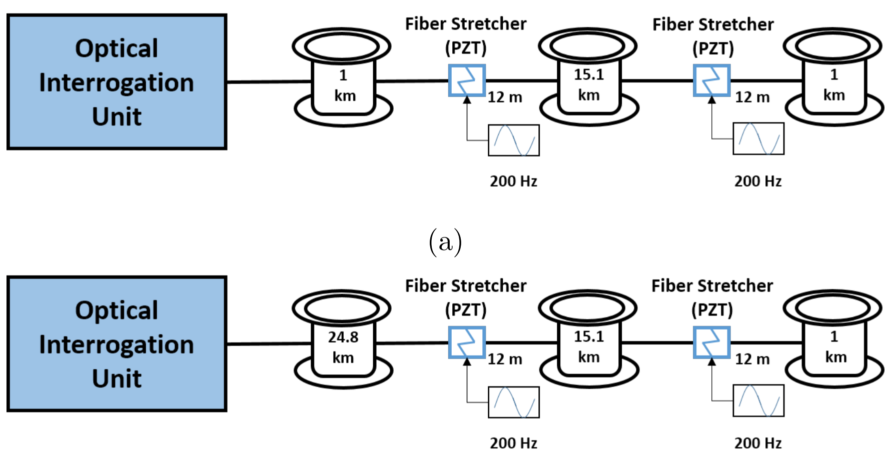

(b)

Figure 4.1: a) Test fiber-1, 17 km, b) Test fiber-2, 41 km.

4.1.2 Parameter Determination

Parameters of the system are determined by the length of the fiber and the desired optical resolution. Interrogation period and repetition rate are limited by the length of the test fiber. It must be greater or equal to the round-trip time of the pulse, i.e. $T_p \geq \tau$. It yields,

$$T_p \geq \frac{2Ln_f}{c} \simeq 410\ \mu s \ \longrightarrow\ T_p = 500\ \mu s \ \Longrightarrow\ f_r = \frac{1}{T_p} = 2\ kHz$$

We chose the interrogation period 500 μs for the sake of simplicity in the computation. Therefore, the maximum detectable acoustic frequency becomes 1 kHz.

Also the desired resolution, Δz, is 10 m. The corresponding pulse duration is calculated as

$$\Delta T = \frac{2n_f \Delta z}{c} \simeq 100\ ns$$

Since the interrogation period is 500 μs and the pulse duration 100 ns, the OTDR trace length, i.e. the number of channels is 500 μs / 100 ns = 5000. The complete list of determined parameters are given in Table 4.2.

Table 4.2: System parameters.

Interrogation period (T_p)	**Repetition rate (f_r)**	**Pulse duration (ΔT)**	**Number of Channels**
500 μs	2 kHz	100 ns	5000

4.1.3 Detection Principle

The PZT vibration induced phase change at the perturbation location can be expressed as

$$\Delta\phi_{PZT}(t) = \frac{V_m \pi}{V_\pi} \sin(2\pi f_m t) \tag{4.1}$$

where V_m and f_m are the voltage and frequency of the PZT drive signal, respectively, and V_π is the half wave voltage of the PZT.

Then using 2.18, the perturbed intensity, I_p, excluding the DC term, can be expressed as

$$\begin{aligned} I_p &= 2 \sum_{j=1}^{N-1} \sum_{k=j+1}^{N} r_j r_k \cos(\phi_j - \phi_k + \Delta\phi_{PZT}(t)) \\ &= 2 \sum_{j=1}^{N-1} \sum_{k=j+1}^{N} r_j r_k \cos(\phi_j - \phi_k + \frac{V_m \pi}{V_\pi} \sin(2\pi f_m t)) \end{aligned} \tag{4.2}$$

Using trigonometric identities yields,

$$I_p = 2 \sum_{j=1}^{N-1} \sum_{k=j+1}^{N} r_j r_k \cdot [\cos(\Phi_{jk} \cos(V_x \sin(2\pi f_m t)) - \sin(\Phi_{jk} \sin(V_x \sin(2\pi f_m t))] \tag{4.3}$$

For the sake of convenience, $\phi_j - \phi_k$ is denoted by Φ_{jk} and $\frac{V_m \pi}{V_\pi}$ is denoted by V_x. Applying the Bessel series expansion to 4.3 yields,

$$I_p = 2 \sum_{j=1}^{N-1} \sum_{k=j+1}^{N} r_j r_k \cdot \left\{ \begin{aligned} &\cos(\Phi_{jk}) \left[J_0(V_x) + 2 \sum_{n=0}^{\infty} J_{2n}(V_x) \cos(2n \cdot 2\pi f_m t) \right] \\ &- \sin(\Phi_{jk}) \left[2 \sum_{n=0}^{\infty} J_{2n+1}(V_x) \sin((2n+1) \cdot 2\pi f_m t) \right] \end{aligned} \right\} \tag{4.4}$$

Equation 4.4 can be reorganized employing the product identities of trigonometric functions,

$$I_p = 2\sum_{j=1}^{N-1}\sum_{k=j+1}^{N} r_j r_k \cdot \begin{bmatrix} 3J_0(V_x)(\cos(\Phi_{jk})) \\ J_1(V_x)\cos(\Phi_{jk} + 2\pi f_m t) - J_1(V_x)\cos(\Phi_{jk} - 2\pi f_m t) \\ J_2(V_x)\cos(\Phi_{jk} + 2\pi 2 f_m t) + J_1(V_x)\cos(\Phi_{jk} - 2\pi 2 f_m t) \\ J_3(V_x)\cos(\Phi_{jk} + 2\pi 3 f_m t) - J_1(V_x)\cos(\Phi_{jk} - 2\pi 3 f_m t) \\ \ldots \end{bmatrix} \tag{4.5}$$

Equation 4.5 indicates the non-linear response of the system to sinusoidal channel perturbations. Intensity signal at the perturbation location contains fundamental tone and its harmonics of which magnitudes are proportional to the Bessel function orders [42]. The equation tells us that as the PZT drive voltage increases, the higher order harmonics will come out; and above certain voltage the power of the fundamental tone will be degraded. It should be noted that the magnitude relation of the frequency components may differ with the effect of fading. For this reason, the non-linearity analysis should be done using the mean SNR parameter which will be explained later in this Chapter.

4.1.4 Experimental Results of PZT Vibration Tests

4.1.4.1 Backscattering traces with and without perturbation

Figure 4.2a and 4.2b show the Rayleigh backscattering traces of the DAS along the first and second fiber under test, respectively, without disturbance. They exhibit a jagged appearance due to the highly coherent light source. For the 17 km test fiber, Fresnel reflection peak can be observed at the end of the fiber. As regards the second trace, since the signal power is very low at the end of the fiber, i.e. 41 km, due to attenuation, the Fresnel reflection peak is not so strong for being observed.

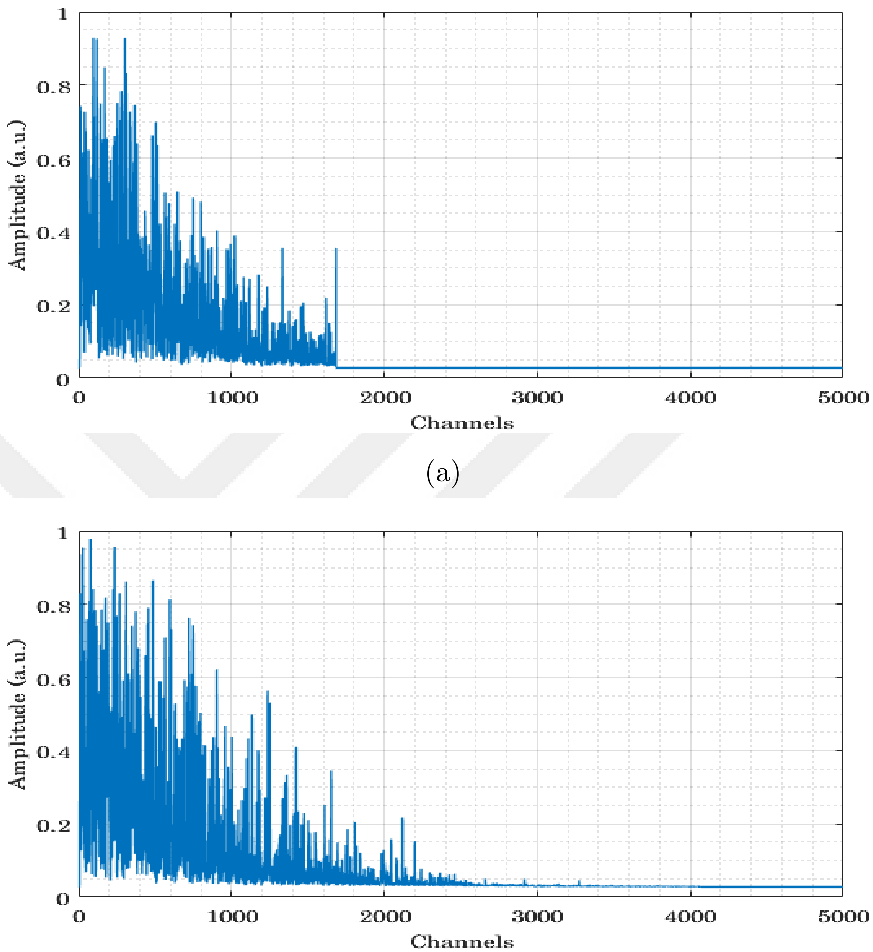

(a)

(b)

Figure 4.2: a) DAS system trace for test fiber-1 (17 km), b) DAS system trace for test fiber-2 (41 km).

After the background signal without perturbation is observed, we inspected the effect of externally applied disturbances along the test fibers. We obtained the location and amplitude of the perturbation by taking the difference of the adjacent traces. Figures 4.3a and 4.3b show the difference data of the backscattering traces of the DAS along test fiber-1 and test fiber-2, respectively, with disturbance. The impact of PZT vibrations can be seen at the test fibers. The two peaks in Figure 4.3a correspond to the two disturbed sections in test fiber-1, i.e. one at the position of 1 km and the other at the position of 16 km. Similarly the two peaks in Figure 4.3b correspond to the two disturbed sections in test fiber-2, i.e. one at the position of 25 km and the other at the position of 40 km.

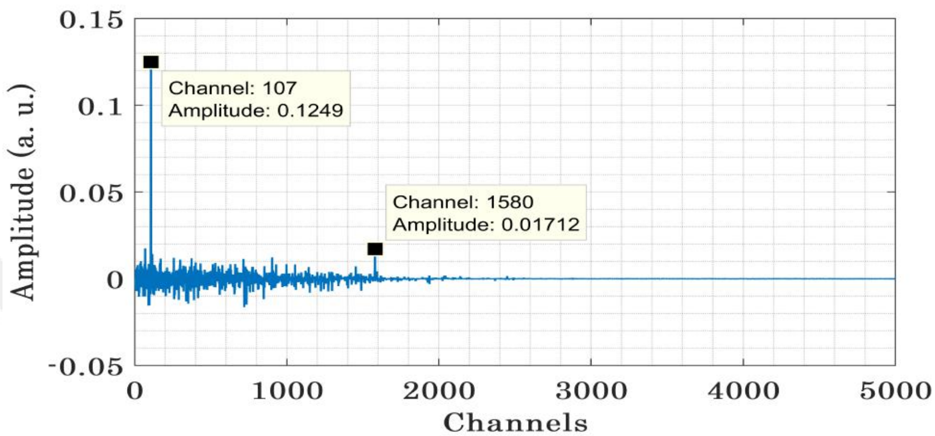

(a)

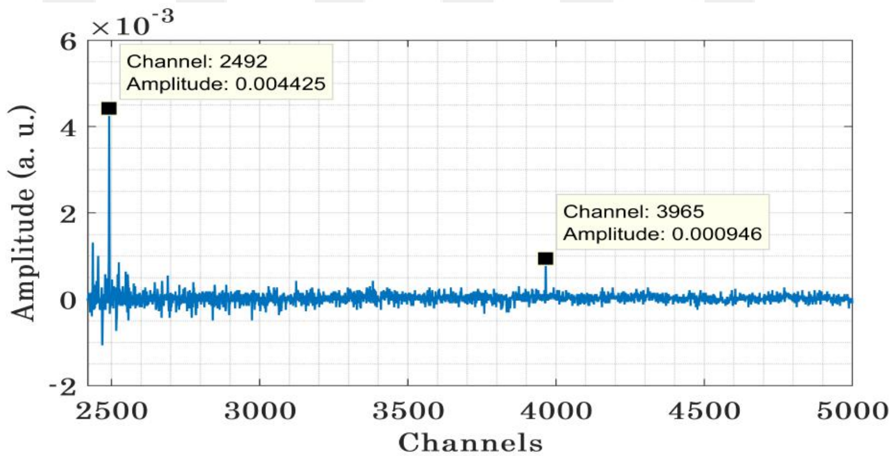

(b)

Figure 4.3: Difference traces showing the impact of PZT vibrations on the fiber for a) test fiber-1 (17 km), and b) test fiber-2 (41 km).

4.1.4.2 Vibration tests with different perturbation signals

To test the ability of vibration detection of the system, different signals were applied on the PZTs with different amplitudes. For this test, difference data at the position of 16 km, corresponding to channel 1580 after digitization, was investigated. The slow-time axis interference signal at the position of 1580 was reconstructed by extracting the corresponding data points from the fast-time axis traces [54], as shown in Figure 4.4. In this manner, the channel data was obtained.

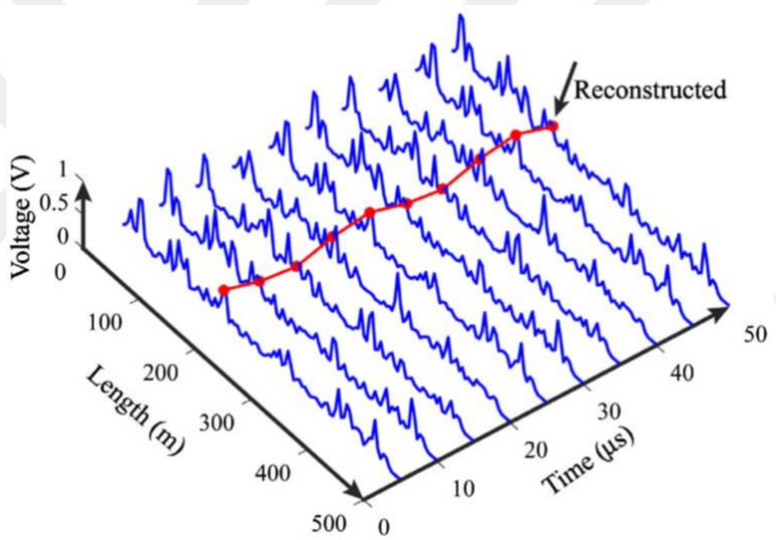

Figure 4.4: Fast-time axis backscattered traces (blue) and slow-time axis channel data (red) [55].

First, a burst signal with a period of 5 sec and 3 cycles of 200 Hz sinusoid was generated by the AWG and applied on the PZT in order to mimic intermittent perturbations. To see the relationship between the amplitude of the applied voltage on the PZT and the corresponding phase change impact on the fiber, we changed the amplitude of the burst signal applied on the PZT. Figures 4.5a and 4.5b show the results for 1 Vpp and 2 Vpp signals, respectively, and Figures 4.5c and 4.5d show zoomed-in sections of the burst signal where 3 cycles of 200 Hz sinusoids can be clearly seen.

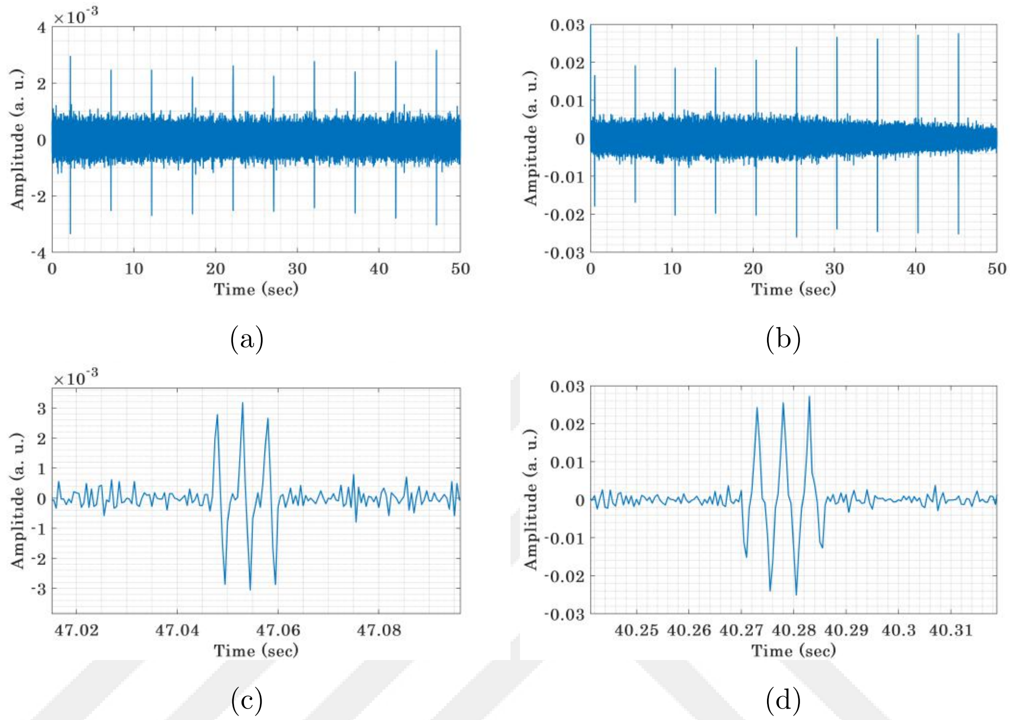

Figure 4.5: Phase change impact of burst signals applied on the PZTs at the distance of 16 km for a) 1 Vpp burst signal, and b) 2 Vpp burst signal. c) Zoomed-in sections of 1 Vpp, and d) 2 Vpp.

Then a sinusoidal signal with a frequency of 200 Hz was applied on the PZTs in order to simulate continuous vibrations. Similarly, different amplitudes of drive voltages were applied on the PZTs, and the results of 0.3 Vpp and 0.5 Vpp signals are plotted in Figure 4.6a and 4.6b. Inset figures clearly show the 200 Hz sinusoidal vibration pattern in the channel data. Figure 4.6c and 4.6d show the power spectrum of the channel data for two voltages, respectively. Since the repetition rate is 2 kHz, maximum detectable frequency of our system is 1 kHz. Clear peaks can be seen at 200 Hz with the harmonics caused by the non-linearity of the system. The power of harmonics increase as the amplitude of the PZT vibration signal goes up.

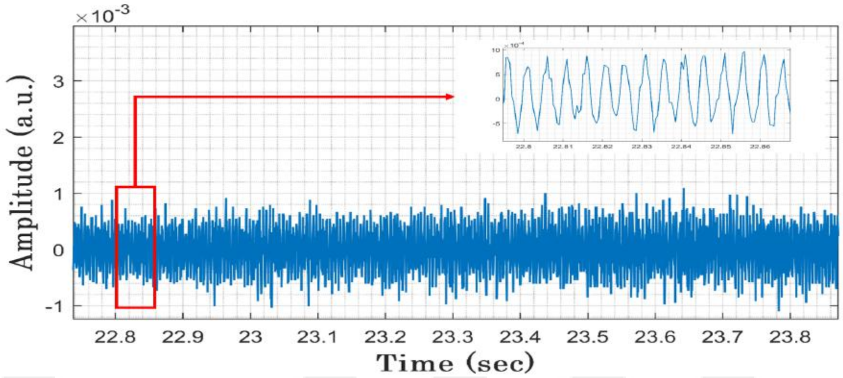

(a)

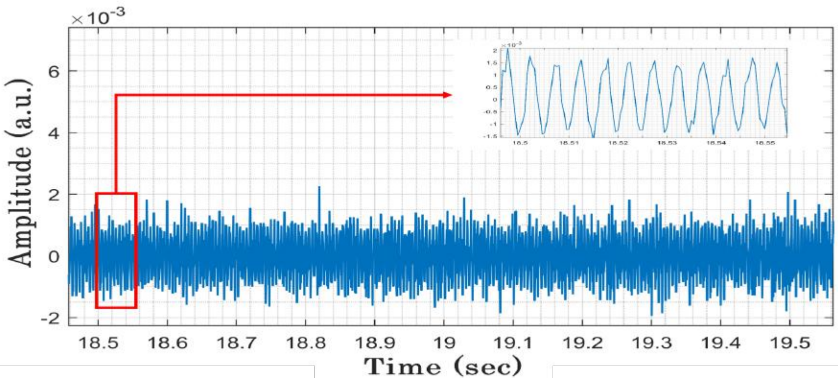

(b)

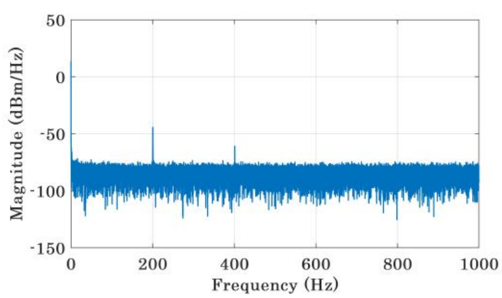

(c)

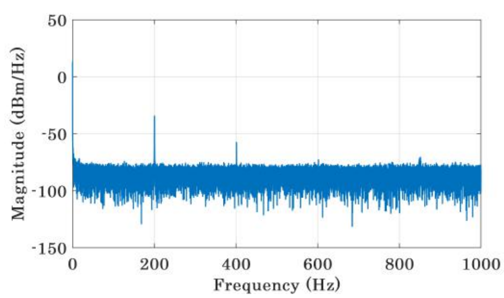

(d)

Figure 4.6: Time domain channel data for a) 0.3 Vpp, and b) 0.5 Vpp. Power spectral densities of channel data for c) 0.3 Vpp, and d) 0.5 Vpp.

4.1.4.3 Different perturbation points along the test fibers

To analyze the range performance of our system as well as testing the ability of sensing simultaneous perturbations in different locations along the fiber; same signal was applied to all of the PZTs. Firstly 3D plots of interference signals around the channels where the disturbances occur were generated in MATLAB. 4 locations of PZTs were plotted separately in Figure 4.7. Here we verify that our system is capable of sensing the intrusion events at distances of 40 km.

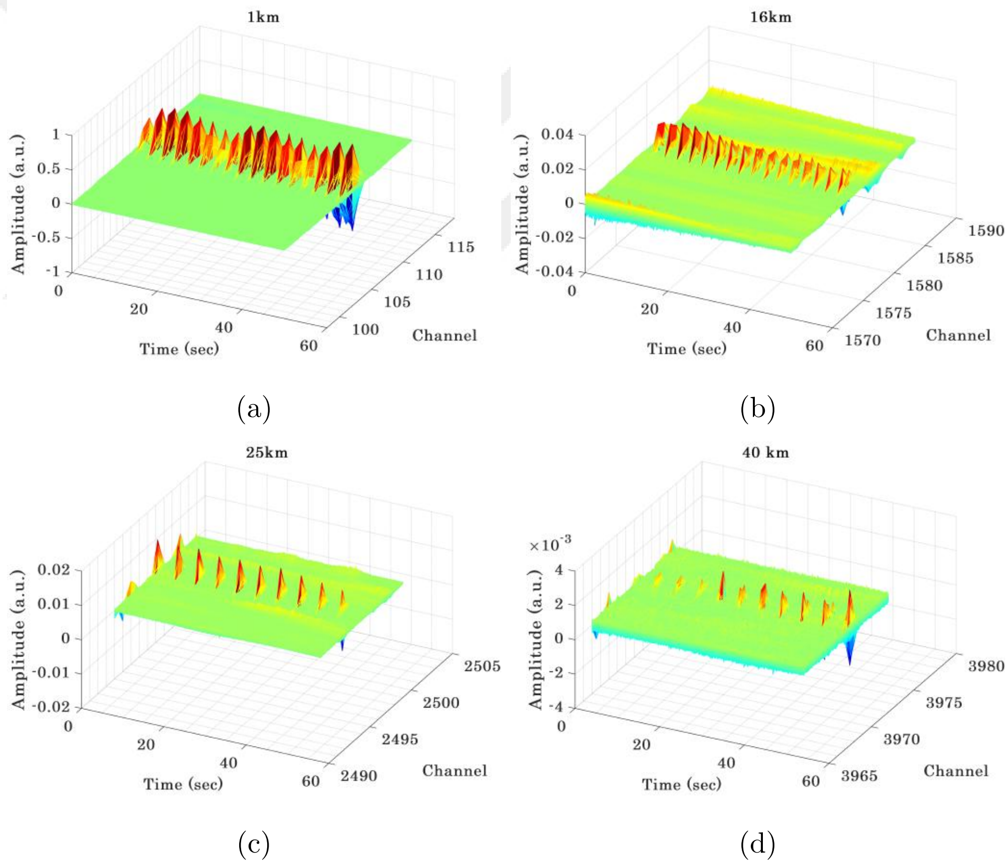

Figure 4.7: 3D plots of channel data for the same burst signal at a) 1 km, b) 16 km, c) 25 km, and d) 40 km.

Then continuous 200 Hz vibration was applied to all of the PZTs. The frequency domain results were plotted for 4 different positions of the fiber, disturbed by the PZTs, in Figure 4.8. The SNRs of the fundamental frequency at channels 107, 1580, 2492, 3966 were calculated as 24.18 dB, 20.11 dB, 11.88 dB, and 8.42 dB. Here the SNR values were calculated as the magnitude ratio between the signal peak amplitude and the background noise level, $SNR = 10 \times \log 10(P_{signal}/P_{noise})$. The number of samples for FFT calculation was 2^{16}.

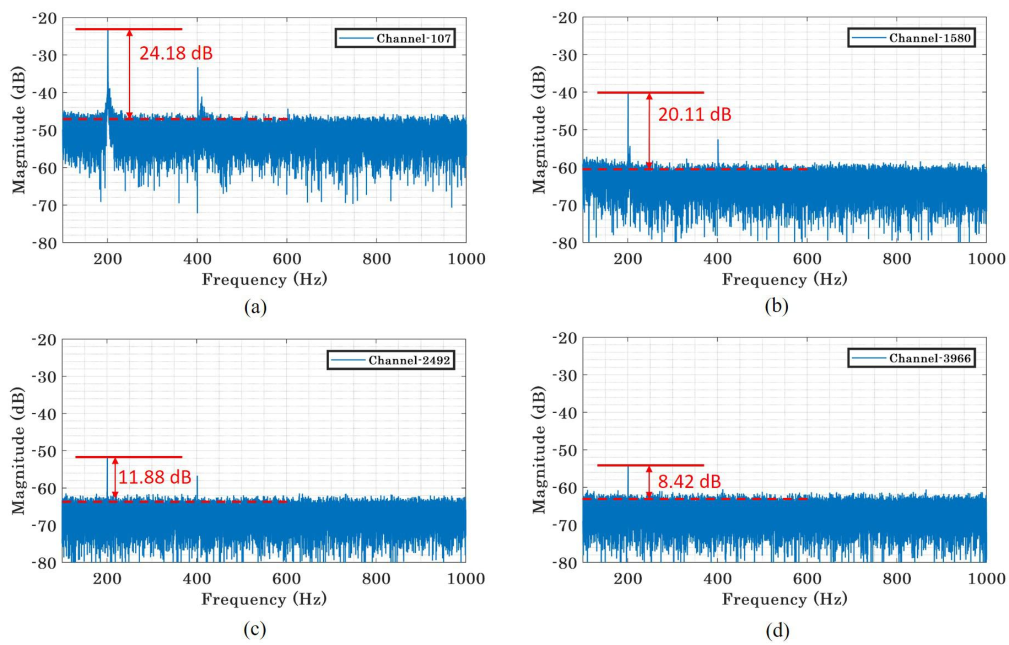

Figure 4.8: Power spectral densities of 200 Hz sinusoidal vibration signal at the positions of a) 1 km, b) 16 km, c) 25 km, and d) 40 km.

4.2 New Figure of Merit: Mean SNR

In this section, we present a new figure of merit to specify the performance characteristics of the direct-detection $\phi-$OTDR based DAS system, which is mean SNR. In fact, in a recent study [28], mean SNR was proposed as a comparison method, however, the analysis is done for a coherent-detection $\phi-$OTDR based DAS system and calculation method differs. Here, we provide a simpler, but hopefully more indicative way of determining and comparing the system performances.

Due to the random nature of Rayleigh backscattered light and fading phenomena, it is hard to characterize the performance of the system. For this reason, the performance of our sensor is specified in a statistical manner in which the mean SNR is determined using the histograms of the SNR. The SNR values are measured for different PZT signals at different locations and the SNR histograms are obtained. The SNR values are extracted from the power spectral density (psd) of the collected data over the monitored fiber span.

For these tests, test fiber-2, i.e. the 41 km long fiber, was used and the distances of 25 km and 40 km were monitored.

50-min data was collected for the first investigations. The interrogation period was the same, i.e. 500 μs, and the applied voltage on the PZTs was 2 Vpp. Time domain data at channels 2492 and 3966 was converted to frequency domain data and the short-time Fourier transform (STFT) analysis was performed with FFT windows of 512. The results are shown in Figures 4.9a and 4.9b, for all the frames, in other words for 50-min duration.

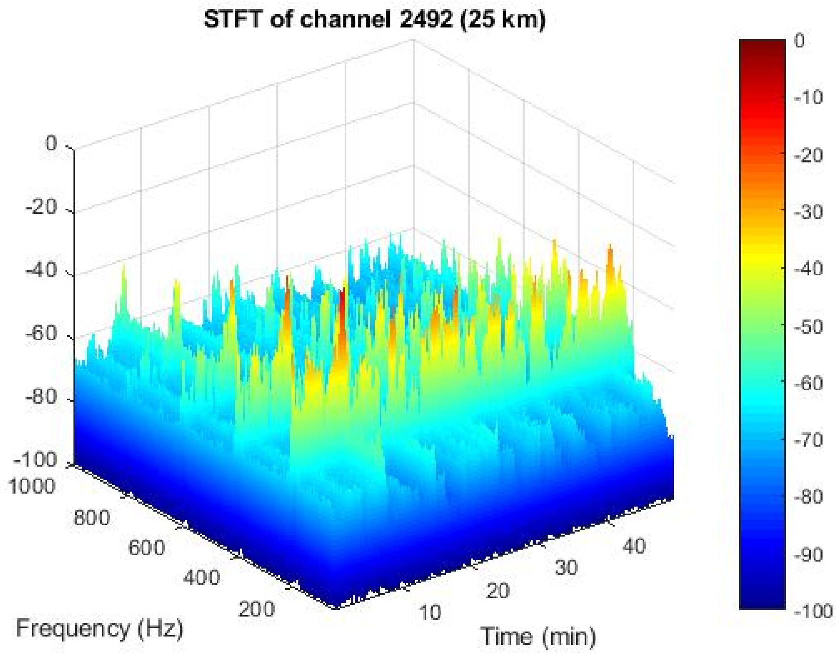

(a)

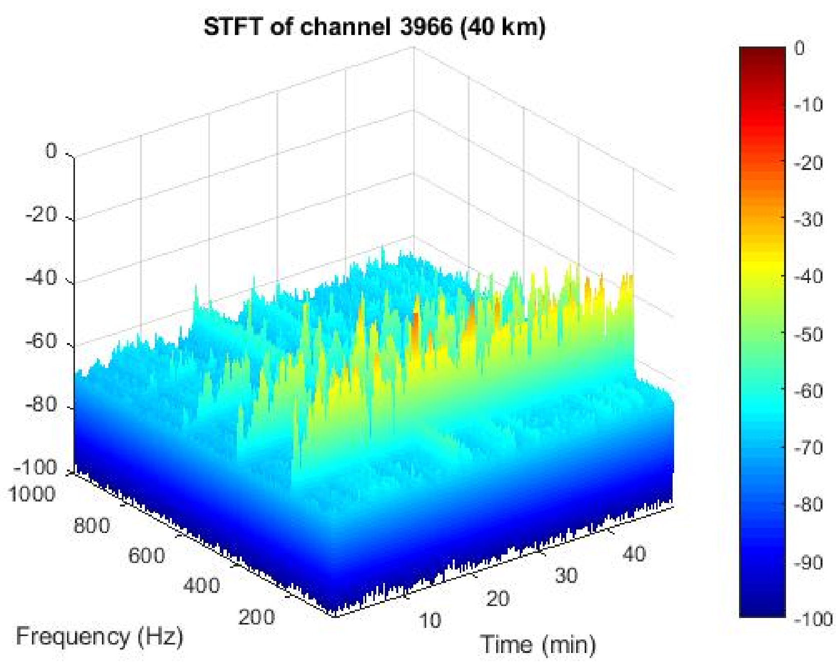

(b)

Figure 4.9: 3D plots of 50-min channel data from a) 25 km, and b) 40 km positions along the fiber.

The 3D STFT diagrams demonstrate that the vibration peaks do not remain the same and they vary in time. Even though the externally applied perturbation is identical, it does not impose the same effect on the backscattered intensity due to the fading effects and non-linear response of the system. The calculated SNRs over 200 Hz peaks, therefore, take different values and the system does not provide a single SNR value for performance assessment. Therefore, considering the variation in SNR, we calculate the SNR values within certain time windows and extract their values in each window. Finally we reach a mean SNR value by averaging all those calculated values.

The mean SNRs at distances of 25 km and 40 km of our system were measured by applying 200 Hz sinusoidal signal on each PZT with voltages varying from 0.025 Vpp to 2 Vpp. Number of FFT points was chosen as 2^{14} while calculating the SNR values. The blue circles and red diamonds in Figure 4.10 show the mean SNR values calculated over the fundamental tone, i.e. 200 Hz at channels 2492 and 3966, corresponding to 25 km and 40 km, respectively. The solid lines correspond to their linear fitting in dB scale. As can be observed from Figure 4.10, the mean SNR increases linearly with the vibration amplitude in dB.

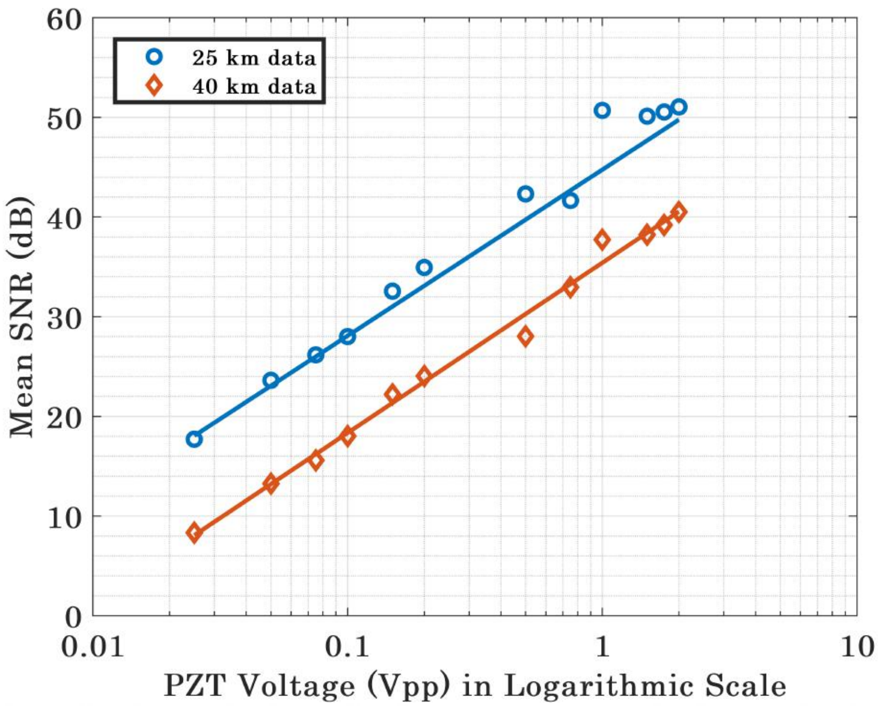

Figure 4.10: The calculated Mean SNR values versus PZT voltages for 200 Hz frequency sinusoidal wave.

In continuing experiments, the stretcher signal voltage was further increased up to 10 Vpp with 2 Vpp steps. The results are shown in Figure 4.11. The mean SNR of the fundamental tone does not keep increasing anymore; but instead it begins decreasing at 25 km position and remains around a certain level at 40 km position. The nonlinear behavior above 2 Vpp may be attributed to the interferometric nature of the system, as formulated in Equation 4.5, in which the power of the fundamental tone transfers to the harmonics. The non-linearity and harmonics analysis is made in the next section.

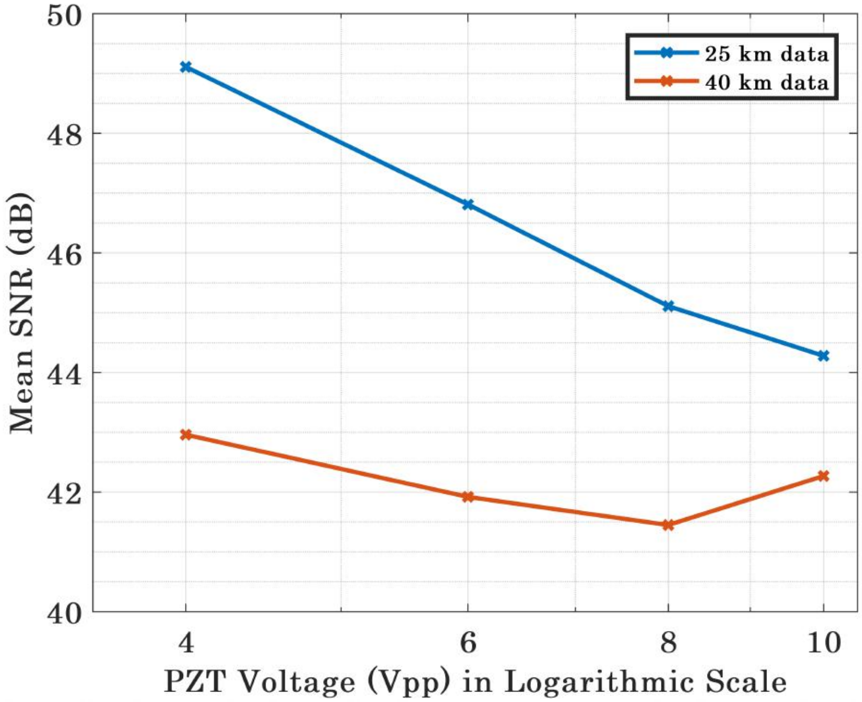

Figure 4.11: The calculated Mean SNR values versus large PZT voltages for 200 Hz frequency sinusoidal wave.

4.2.1 Non-linearity and Power Transfer to the Harmonics Analysis

We performed a large signal analysis and investigate the non-linearity of the system and the power transfer to the harmonics.

For this purpose, mean SNRs were calculated over three different frequency peaks. The first value was obtained from the fundamental frequency itself as done in the previous calculations. The second value was obtained from the first harmonic, i.e. the peak around 400 Hz. And the third value was obtained by summing the powers of all harmonics and then taking its ratio to noise level. The results of each calculations were named Fundamental SNR, Harmonic SNR and Overall SNR, respectively.

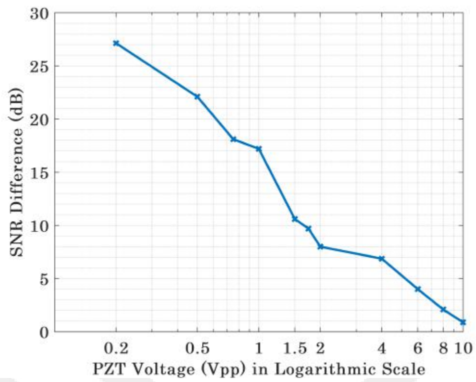

(a)

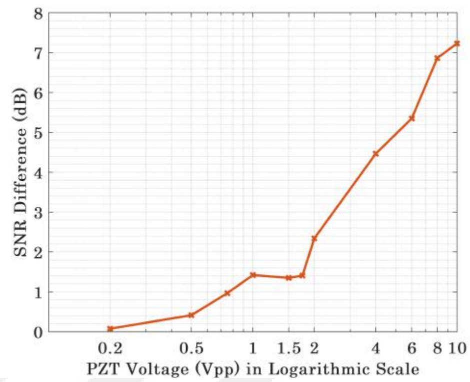

(b)

Figure 4.12: a) Mean SNR difference between Fundamental SNR and Harmonic SNR, b) Mean SNR difference between Fundamental SNR and Overall SNR.

The difference between Fundamental SNR and Overall SNR and the difference between Fundamental SNR and Harmonic SNR with respect to increasing PZT voltages are plotted in Figures 4.12a and 4.12b, respectively. For this analysis, we focused on the vibration at 25 km position.

Below we list some of our observations regarding the experimental results presented above.

- As the PZT voltage increases, the difference between Fundamental SNR and Harmonic SNR decreases. Thus, the amount of power transfer to the harmonics and thereby the non-linearity increases.
- In parallel with this, the difference between Overall SNR and Fundamental SNR increases, indicating that the linear response of the system to the PZT vibrations impairs as the PZT voltage increases. Thus, the error level of the mean SNR, which is calculated by considering only the fundamental frequency, gets higher.
- Even though the difference between Overall SNR and Fundamental SNR is increasing, a maximum SNR difference of 2 dB is observed in the range of 0.2-2 Vpp. Therefore, below 2 Vpp, the mean SNR, calculated over the fundamental tone, seems to be an appropriate performance metric at an

acceptable error level. However, since this difference for larger PZT voltages exceeds 3 dB, the analysis should be made by taking into consideration all the harmonics and an accordingly defined performance metric should be provided; or certain linearization methods have to be implemented to the system.

We also investigated the distributions of Fundamental SNR and Overall SNR for all PZT voltages. The distributions for the smallest and largest PZT voltages are presented in Figures 4.13a and 4.13b for comparison. In consistent with the observations above, the distributions of Fundamental SNR and Overall SNR do not show much difference at smaller voltages, whereas at larger voltages the distributions shift to the right and tighten up significantly, implying that fading decreases. The corresponding Fundamental SNR and Overall SNR values for 0.2 Vpp and 10 Vpp km are 34.4 dB, 35.02 dB and 44.48 dB, 51.51 dB, respectively.

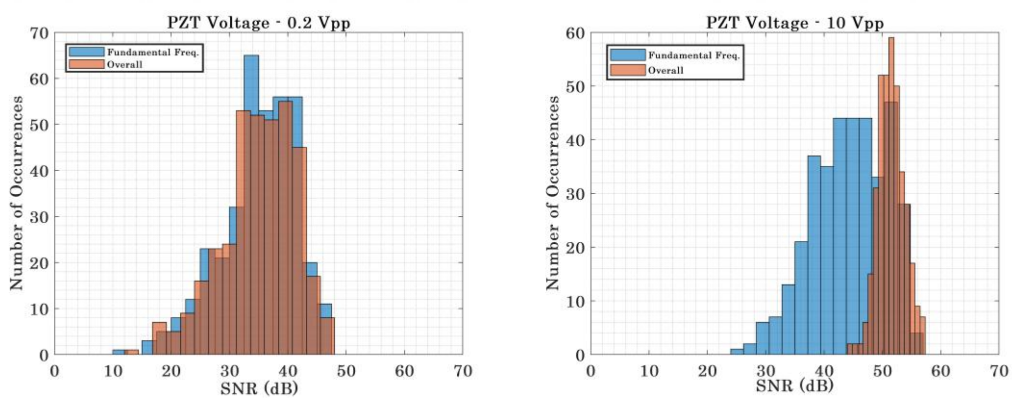

(a) (b)

Figure 4.13: Histograms of Fundamental SNR and Overall SNR for a) 2 Vpp, and b) 10 Vpp.

4.3 Statistics of Rayleigh Backscattered Signal in the Presence of ASE Noise

As previously mentioned, the return signal at the input end of the fiber exhibits a speckle-like appearance which results from the coherent superposition of light from the scatterers within the pulse duration [56]. It is a form of multi-point interference, similar to the phenomenon which is observed in conventional microwave radar and communications systems [1]. In direct-detection $\phi-$OTDR systems this phenomenon is generally referred to the exponential fading [57] and characterized by the negative exponential distribution. In the presence of amplified spontaneous emission (ASE) noise from the optical preamplifier, the characteristics of the distribution departs from the negative exponential probability density function (pdf) and is better represented by ex-Gaussian pdf. This section presents the theoretical background of the speckle noise in the presence of ASE noise, then demonstrates the experimental results and validates the developed statistical characteristics of the backscattered intensity. In the final part, the effects of ASE noise for a direct detection system is investigated under a perturbation test and shown that ASE noise can impair the system performance up to $\backsim$18 dB.

4.3.1 Calculations

Both laser speckle patterns in spatial domain and Rayleigh backscattered signal patterns in time domain result from the random multipoint interference of highly coherent beams and hence have similar statistical behavior which is derived in [58]. The physics of speckle, generated by the scattering from the rough surfaces, can be considered similar to the one generated by the Rayleigh scattering from the scatterers in the fiber [1]. The statistics of the intensity of a speckle field at a channel is represented by the negative exponential distribution [59]. It assumes that the degree of freedom, which is the estimate of statistically independent field components, is one for single-mode fiber, single-frequency source, and single-polarization state [1]. The pdf of backscattered light intensity (I_{BS}) is given by [59]

$$p(I_{BS}) = \frac{e^{-I_{BS}(z)/\langle I_{BS}(z)\rangle}}{\langle I_{BS}(z)\rangle} \tag{4.6}$$

where $I_{BS}(z)$ is the backscattered intensity from distance z and $\langle I_{BS}(z)\rangle$ is the average intensity.

ASE noise appears in the optical systems in two main forms, the ASE-ASE beat noise and the ASE-signal beat noise, and these noises are given by

$$i^2_{ASE-ASE} = 4\mathcal{R}^2\rho^2_{ASE}B_{opt}B \tag{4.7a}$$

$$i^2_{ASE-sig} = 4\mathcal{R}^2 G I_{BS}\rho_{ASE}B \tag{4.7b}$$

where $\mathcal{R}$ is the responsivity of the photodetector, ρ_{ASE} is the ASE spectral density, B_{opt} is the optical bandwidth, B is the electrical bandwidth and G is the amplifier gain.

The other noise components which are not included here are the ASE-shot noise and the signal-shot noise components. Since the ASE-ASE beat noise and the ASE-signal beat noise components are much larger and dominant for a high-gain optical amplifier, these noises are ignored [60].

It is a common practice to use Gaussian approximation for the distribution of the optical amplifier ASE noise for statistical calculations in optical systems [36, 60, 61]. This approximation is also employed in this paper for simplicity. Therefore, the ASE-ASE noise and the ASE-signal noise can be treated as independent Gaussian stochastic processes and the statistical properties of the amplifier noise can be described by the total variance given by $\sigma^2_{ASE} \approx i^2_{ASE-ASE} + i^2_{ASE-sig}$ [60].

Combining all together, the amplifier noise follows a non-centered Gaussian distribution and the Rayleigh backscattered signal itself follows a negative exponential distribution. The resulting distribution is obtained by convolving the negative exponential pdf and Gaussian pdf which yields the ex-Gaussian pdf with the following parameters:

$$p(I_{BS}) = \frac{1}{\langle I_{BS}(z)\rangle} \exp\left(\frac{\mu_{ASE}}{\langle I_{BS}(z)\rangle} + \frac{\sigma_{ASE}^2}{2\langle I_{BS}(z)\rangle^2} - \frac{I_{BS}(z)}{\langle I_{BS}(z)\rangle}\right) \Phi\left(\frac{I_{BS}(z) - \mu_{ASE} - \frac{\sigma_{ASE}^2}{\langle I_{BS}(z)\rangle}}{\sigma_{ASE}}\right) \tag{4.8}$$

where the parameters μ_{ASE} and σ_{ASE} correspond to the mean and standard deviation of the Gaussian component and the function symbolized by Φ is the error function.

Equation 4.8 shows that the pattern of the backscattered signal distribution depends on the optical bandwidth and the position along the fiber.

4.3.2 Experimental Set-up and Results

The experimental set-up designed to obtain empirical evidence relevant to this problem is shown in Figure 4.14. The same highly coherent narrow linewidth continuous-wave (CW) laser is used as the light source. An acousto-optic modulator (AOM) which is placed after a booster erbium doped fiber amplifier (EDFA) generates the 100 ns interrogation pulses which are injected into the fiber via a circulator. The backscattered signal from the fiber is directed to a preamplifier EDFA via the same circulator and then split into three branches via optical couplers. Each branch includes a variable optical attenuator (VOA) to adjust the power level for fitting into the min-max regimes of the photodetectors. The detected signals from three branches are simultaneously acquired by a data acquisition system and then post-processed in a PC to analyze the statistical characteristics.

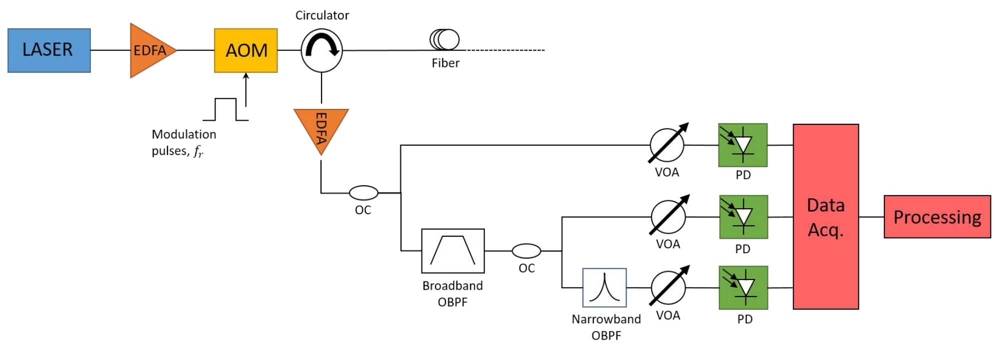

Figure 4.14: Experimental setup. EDFA: Erbium doped fiber amplifier, AOM: Acousto-optic modulator, OC: Optical coupler, OBPF: Optical band pass filter, VOA: Variable optical attenuator, PD: Photodetector, Data Acq.: Data Acquisition.

In the first branch the output signal from EDFA is directly sent to the photodetector without filtering in order to analyze the statistical characteristics of the case where the ASE-ASE noise is the largest. In the second branch the output signal from EDFA is filtered by a broadband optical band-pass filter (OBPF) (0.22 nm bandwidth Add/Drop filter) before the photodetector in order to analyze the statistical characteristics of the case where the ASE-ASE noise is lower. Similarly, in the third branch an additional narrowband OBPF (0.02 nm bandwidth 25 GHz F-P Filter) is employed after the broadband OBPF in order to analyze the statistical characteristics of the case where the ASE-ASE noise is the lowest. We name these cases as EDFA, Broadband OBPF and Narrowband OBPF, respectively. The same experimental setup is used for the perturbation tests.

For each case, we simultaneously recorded the full traces of the data from three photodetectors with 5000 channels, covering 50 km length of the single-mode optical fiber sensor (10 meter per channel). In order to restrict the number of degrees of freedom to 1, we took a very short interrogation time where the laser frequency drifts or polarization state changes are negligible.

We investigated both the signal coming from near channels [1-1000], corresponding to 1-10 km and farther away channels [3000-4000] corresponding to 30-40 km. We generated the intensity distribution histograms of the backscattered signals and the results are shown in Figures 4.15 and 4.16 for near channels and farther away channels respectively.

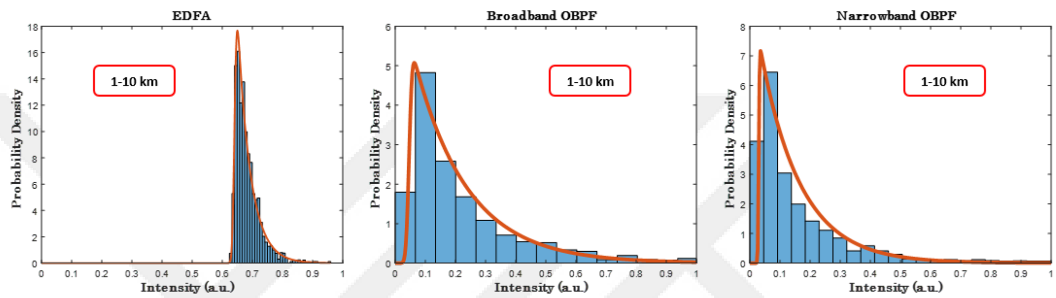

Figure 4.15: Histograms of the intensity distributions of the backscattered signals from channels [1-1000] and ex-Gaussian fittings for EDFA (Left), Broadband OBPF (Middle) and Narrowband OBPF (Right) cases.

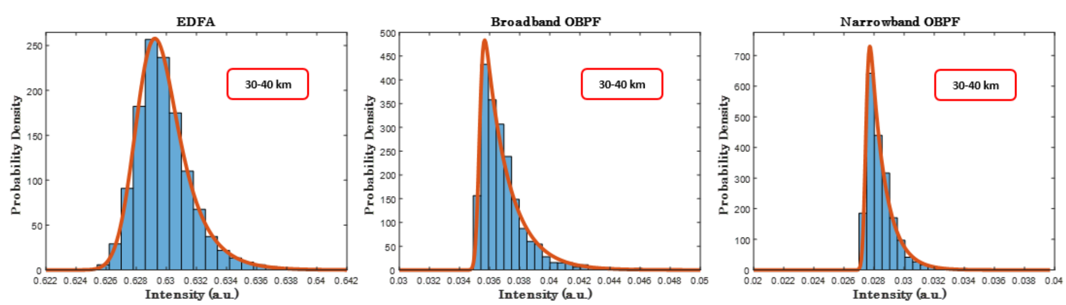

Figure 4.16: Histograms of the intensity distributions of the backscattered signals from channels [3000-4000] and ex-Gaussian fittings for EDFA (Left), Broadband OBPF (Middle) and Narrowband OBPF (Right) cases.

The results show that the distributions can be characterized well by ex-Gaussian pdfs. The parameters for the ex-Gaussian distribution depend on the position along the fiber and the amount of ASE noise, in other words the bandwidth of the OBPF. Comparison to the fitting curves of the intensity pdfs shows good fit with the experimental data. It is important to note that the ex-Gaussian distributions are non-centered, i.e. having non-zero offset, due to the ASE noise added DC component.

Depending on the ratio between the signal intensity and ASE noise, the ex-Gaussian parameters vary and the distributions take different shapes. If ASE noise is dominant, as in the EDFA case or at large distances, the distribution converges to non-centered Gaussian distribution. On the other hand, if the signal intensity is dominant as in the Narrowband OBPF case or at the small distances, the distribution converges to non-centered negative exponential distribution. In this sense, the results demonstrate the dependence of statistical properties of Rayleigh backscattered signals on the position and the bandwidth of the OBPF in the presence of ASE noise.

4.3.3 Perturbation Tests in Three Configurations

We also investigated the effect of ASE noise on the system performance using the same setup shown in Figure 4.14. Also the second test fiber shown in Figure 4.1a was used in which two identical fiber stretchers are placed at the positions of 25 km and 40 km. The stretchers were driven with 200 Hz sinusoidal signal which creates perturbations at the same frequency. The perturbations were recorded with the optical interrogator and the mean SNR values were calculated using the method previosly described in 4.2. The mean SNR values for each case for 25 km and 40 km are shown in Figure 4.17.

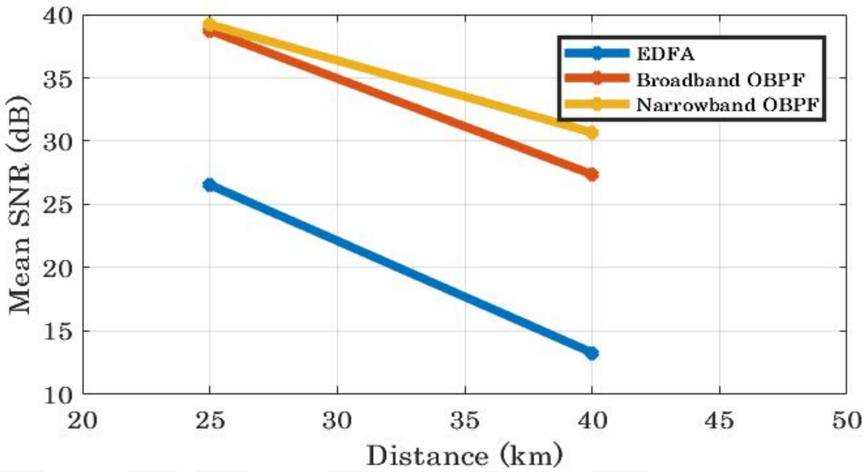

Figure 4.17: Mean SNR values for EDFA, Broadband OBPF and Narrowband OBPF cases.

The results show that, filtering ASE noise can improve the system performance up to 18 dB at 40 km distance. Also the effect of ASE noise increases with distance; for 25 km the SNR value of Broadband OBPF and Narrowband OBPF are nearly identical. However at 40 km, there is nearly 4 dB SNR improvement with narrower filtering. The system is limited by other noise sources at small distances, which we are still investigating.

Chapter 5

Field Tests and Results

A field demonstration of the DAS system over a buried cable was performed around the NANOTAM facility with a 100 m of rectangular perimeter, as shown in Figure 5.1.

Figure 5.1: Test field with buried fiber cables around NANOTAM facility.

For the field tests, the same experimental configuration as in the laboratory tests was used. This time a ∽51 km-long single-mode fiber is used as the sensing cable of which certain portions were buried under the soil. The sensing fiber was divided into 11 sections as shown in Figure 5.2. Sections B, D, F, H and J were placed in an isolated box in the laboratory, which insulates the fiber spools from thermal and acoustic effects. The sections A, C, E, G, I and K were buried with the same depth (1 m) and length (100 m) in the field after their certain lengths (150 m) pass through the building. These sections are bundled in the same fiber optic circumscribe the same In this manner the distances of ∽100 m, ∽12 km, ∽21 km, ∽30 km, ∽40 km and ∽50 km were able to be monitored simultaneously.

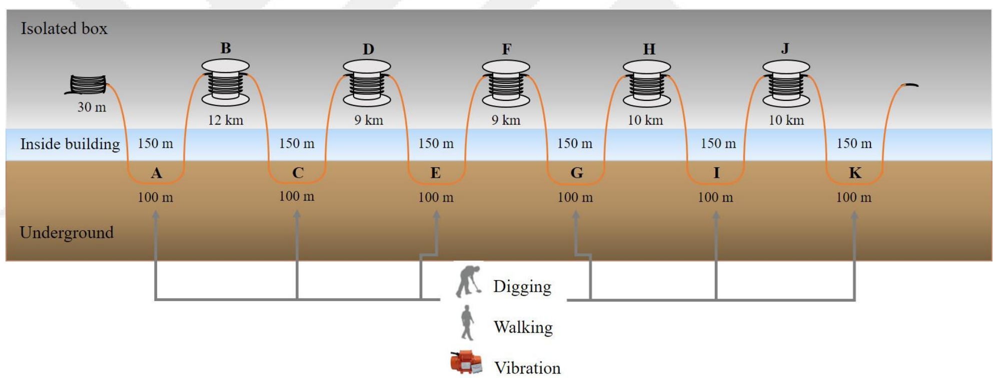

Figure 5.2: Sensing fiber link and field test configuration for DAS system.

The interrogation period was increased to 515 μs, in order to cover ∽51 km, and the pulse width remained the same, i.e. ∽100 ns, corresponding to a ∽10 m spatial resolution. This yielded 5150 samples for each interrogation.

The series of tests were conducted to evaluate the system performance and to obtain a better indication of reliability of the sensor. Tests were carried out to investigate the response of the sensor system to different intrusion events such as digging, walking and motor vibration. These tests are explained in the following sections.

5.1 Digging Tests

The first intrusions were conducted by digging activities in proximity to the buried fiber. The data was recorded as a person stroke the ground with a pickaxe at certain distances from the edge of the buried cable. We first located the positions of the perturbation for 6 regions along the buried fiber. The maximum intensity differences occurred at channels 15, 1253, 2157, 3085, 4087, and 5002 for the distances of 100 m, 12 km, 21 km, 30 km, 40 km, and 50 km, respectively. Then we examined the characteristics of the fluctuation in the Rayleigh backscattered signal that the digging activity caused.

We acquired multiple datasets by varying the system parameters such as the EDFA currents or pulse width, and changing the lateral distance of the digging activity to the fiber as well as changing the frequency and strength of the strikes. As one illustration, we plotted one hour raw data of a perturbed channel collected during a digging test in Figure 5.3. Here in this test the digging frequency is 3.5 min (number of separate digging events is 17). It can be observed from the inset of Figure 5.3 that the digging perturbation manifests itself as an exponentially decaying sinusoid on the interference signal.

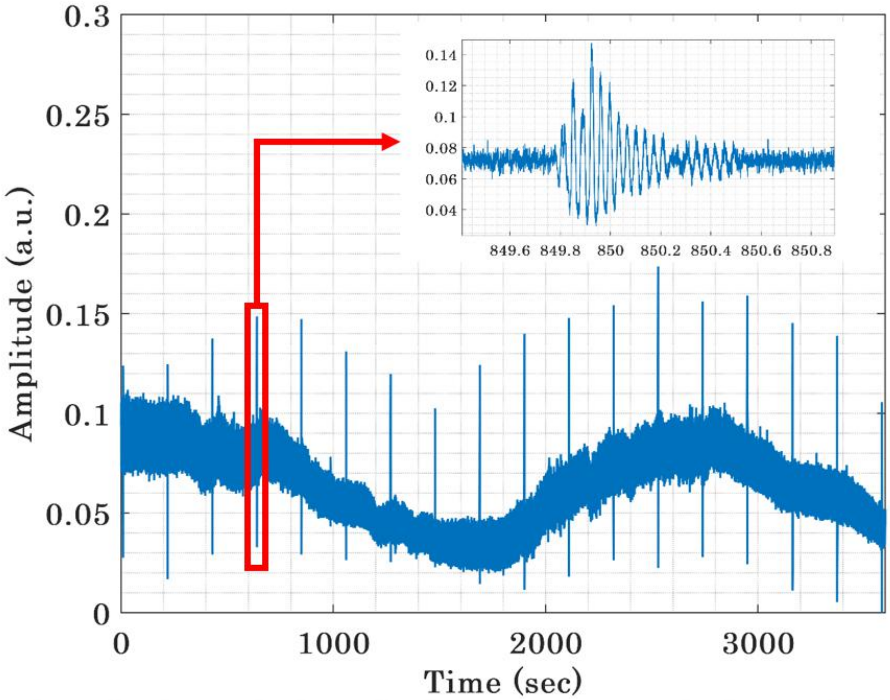

Figure 5.3: Digging activity results.

We then made a spectrogram analysis with DFT windows of 1024 to extract the spectrum of frequencies of the interference signal as they vary with time and to see the amount of power in each frequency band. For the sake of convenience, only the time instances that the perturbation occurs were selected.

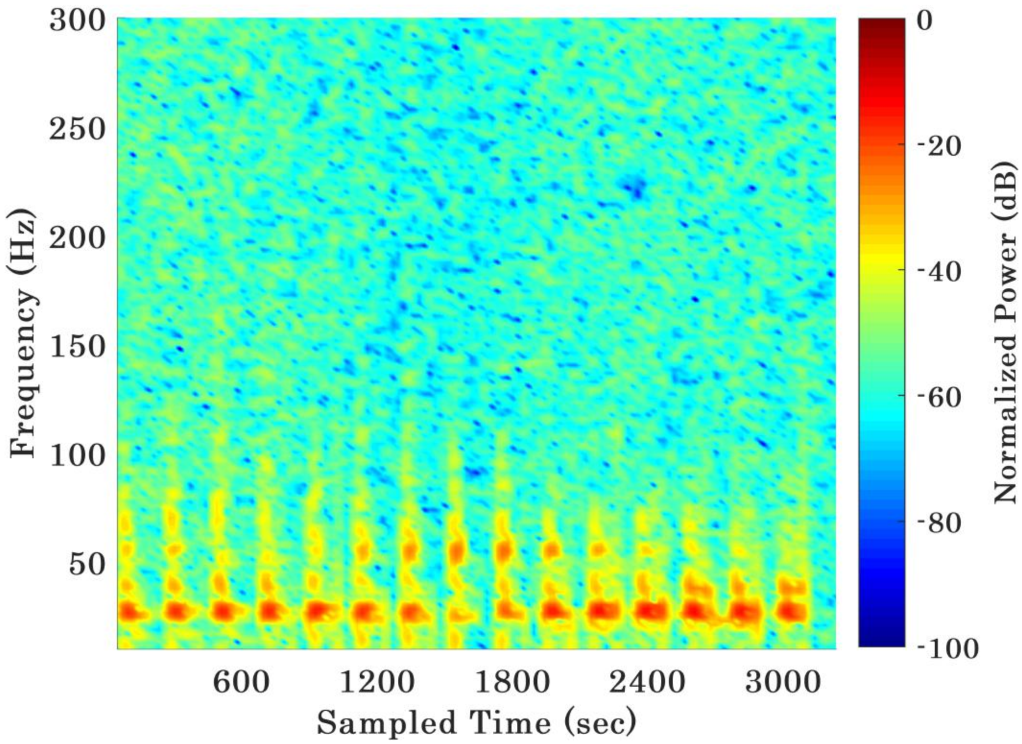

Figure 5.4: The intensity map with frequency information of the digging event at the certain position along the sensing fiber.

It can be observed from Figure 5.4 that most of the power is concentrated at frequencies between 25 Hz and 80 Hz, peaks occurring around 27.5 Hz and 55 Hz. Therefore, we performed further analyses by implementing a simple signal processing algorithm in which the channel data passes successively through a sequence of processing steps including:

- **Differencing:** As usual, firstly difference of adjacent samples are taken in order to detect the location and phase change impact of the perturbation.
- **Windowing:** The samples are windowed to better distinguish the peaks caused by digging events.
- **Bandpass filtering:** The bandpass filter is applied to the samples in the windows to reduce the noise and eliminate the uninterested frequencies.

The low cut-off frequency of the bandpass filter is 25 Hz and high cut-off frequency is 80 Hz.

- **Square-summing:** The filtered samples are squared point by point and then summed to compute the total power within the 25-80 Hz band falling into that window.

We performed further digging tests with varying parameters and conditions; and analyzed the detection performance of our system using this algorithm. In the following test results illustrated in Figure 5.5, a set of 400 sec data was collected with a 10 m of lateral distance to the buried fiber and a digging frequency of 35 sec (number of separate digging events is 12). According to results, in the first 5 regions, i.e. at the distances of 100 m, 12 km, 21 km, 30 km, and 40 km, all of the strikes were clearly detected with acceptable SNR levels above the noise. However, at the distance of 50 km the strikes were barely detected, which indicates that the system requires performance improvement.

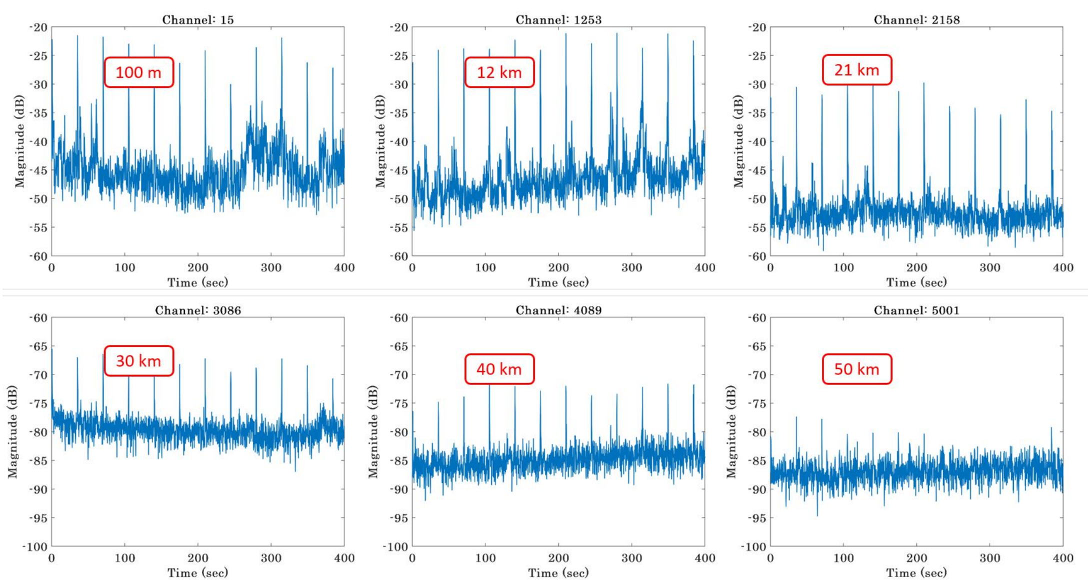

Figure 5.5: Detected digging events in 6 regions.

5.2 Walking Tests

The next intrusions were conducted by walking along the buried fiber path on the test field. The data was recorded as a person stepped on the ground above the buried fiber, walking along the rectangular path of 100 m perimeter.

Since the frequency signature of the walking event is similar to that of the digging event except being weaker and experiencing faster exponential decaying, the same algorithm and bandpass filtering was applied to the channel data. The results of the first 4 regions were illustrated in Figure 5.6. The color maps were adjusted for each region individually for better visuality. The peaks are visible along 10 channels for each region in a shifting fashion from left to right on the channels, representing walking along the 100 m rectangular path. Also from figures, it is seen that at the starting and end locations of the fiber path, i.e. at around 5 sec and 85 sec, the peaks appear in both channels since this is the joint point of the fiber cable making loop-back. These are shown by red circles in the Figures.

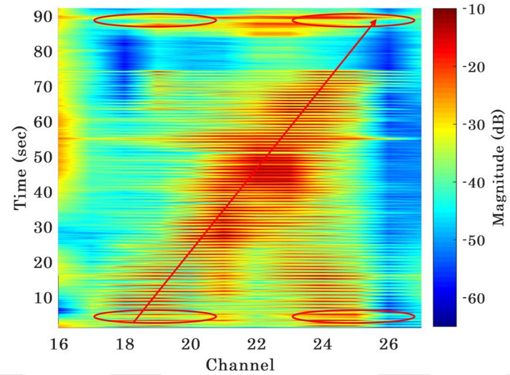

(a)

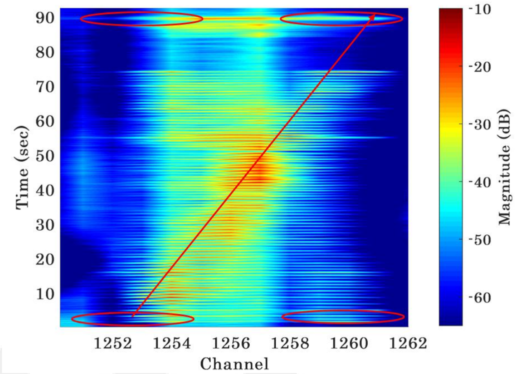

(b)

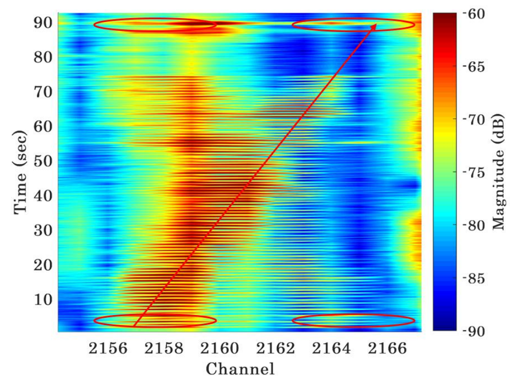

(c)

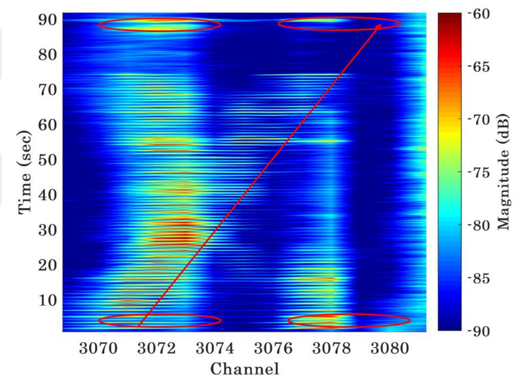

(d)

Figure 5.6: Detected walking events in the first 4 regions, i.e. at the distances of a) 100 m, b) 12 km, c) 21 km, d) 30 km.

To monitor the distances of 40 km and 50 km the preamplifier gain was maximized, since otherwise the backscattered intensity was very weak. The results of the last 2 regions were illustrated in Figure 5.7 exhibiting similar patterns as observed in the first 4 regions.

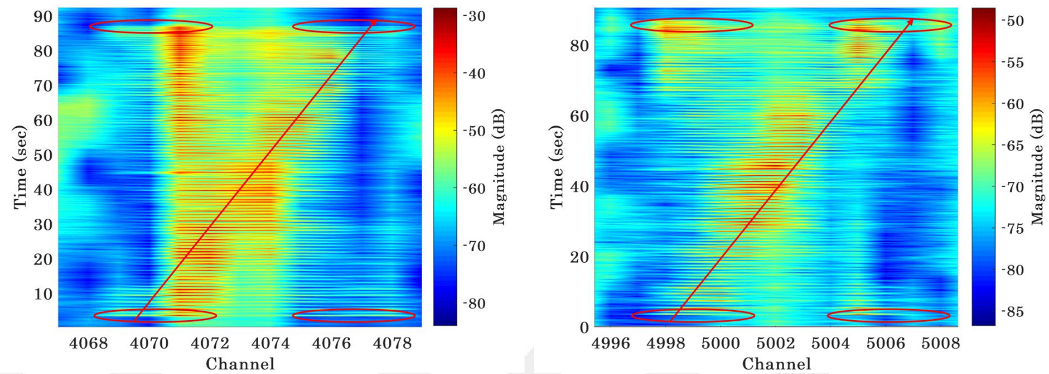

(a) (b)

Figure 5.7: Detected walking events in the last 2 regions, i.e. at the distances of a) 40 km, b) 50 km.

5.3 Vibration Tests and Fading Measurements

After digging and walking events were shown to be successfully detected by our sensor system, we performed vibration tests to better understand the statistical properties of the system and examine fading effect. In this section, we experimentally show the statistical characteristics of the SNR of our direct-detection DAS system, calculated over five days and 48 hours of data acquired from the field. We also demonstrate the distribution patterns of SNR in different distances and the change in mean SNR over distance.

Vibration tests were conducted on the same test configuration. To test the ability of the system of sensing a vibration event, ∽50 Hz sinusoidal signal was applied to the buried fiber generated by a motor which is placed 3 m away from the buried fiber and time-domain traces of the specific samples were collected over the monitored distances.

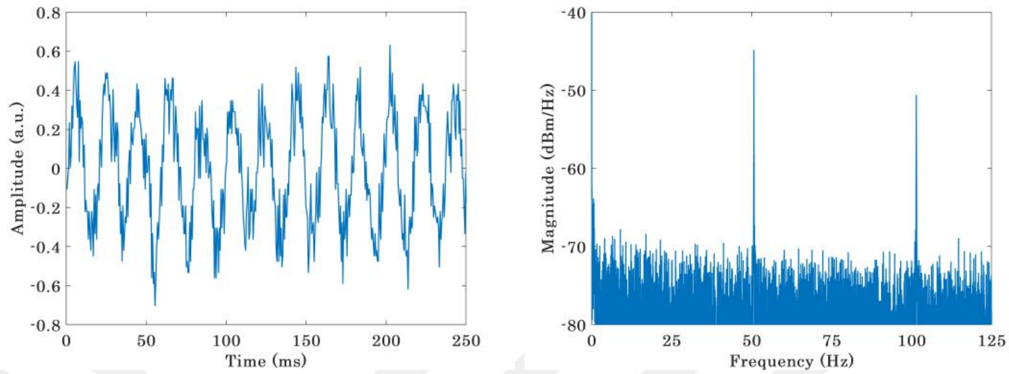

(a) (b)

Figure 5.8: a) Time trace and b) spectrum of a 50 Hz vibration signal at 21 km.

We measured the vibration signal within five different days over the course of about 10 hours in each day, i.e. total of 48 hours, for obtaining a single mean SNR value. Using the calculation method and analysis described in Section 4.2, the time-domain data shown in Figure 5.8a was converted to frequency domain and their power spectral densities were calculated. SNR value was extracted from the ∽50 Hz peak of the psd data shown in Figure 5.8b. Since the amplitudes of the vibration events are varying in time due to fading, SNR values were calculated in certain time windows. The number of samples over which SNR values were calculated was selected 2^{16} for the sake of convenience, which corresponds to time windows of 33.75 seconds. This resulted in arrays of SNR values which have ∽5000 elements for each monitored distance. Using these arrays, histograms of SNR values at these distances were generated and shown in Figure 5.9.

The results presented in Figure 5.9 reveal the probabilistic nature of the system. It results in different SNR values under different conditions varying in time. For example, the SNR starts from 30 dB and goes up to 80 dB at the 100 m position whereas it varies between 5 dB and 35 dB at the 50 km position. Also, it is seen that the heights of the histogram bins get smaller as the distance increases, in other words, the number of occurrences starts to distribute more uniformly and become more spread. This implies that at long distances fading becomes more significant.

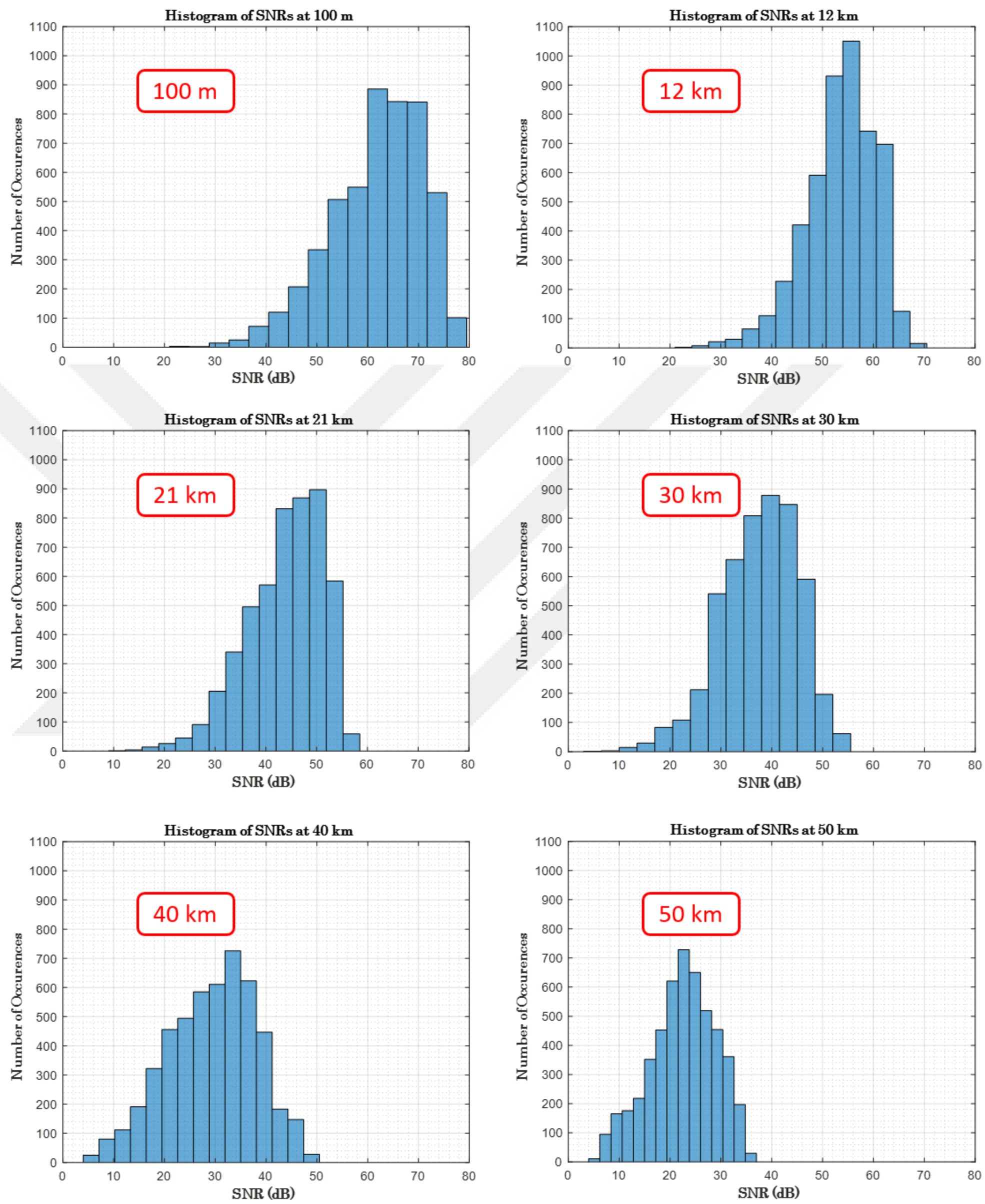

Figure 5.9: Histograms of SNRs at distances 100 m, 12 km, 21 km, 30 km, 40 km and 50 km.

The results show that the SNR value has probabilistic fashion and cannot be identified as a single value for a given distance. In order to have a good estimation about the system performance, the shape of the probability distribution function (pdf) should also be taken into consideration. Therefore, the mean SNRs were determined over the distributions shown in Figure 5.9 and the change in mean SNRs over distance are presented in Figure 5.10. The mean SNR values show a linear decrease for longer distances as expected. The decrease is around 8 dB/10km (in electronic domain), which is consistent with a fiber loss of 0.2 dB/km (in optical domain).

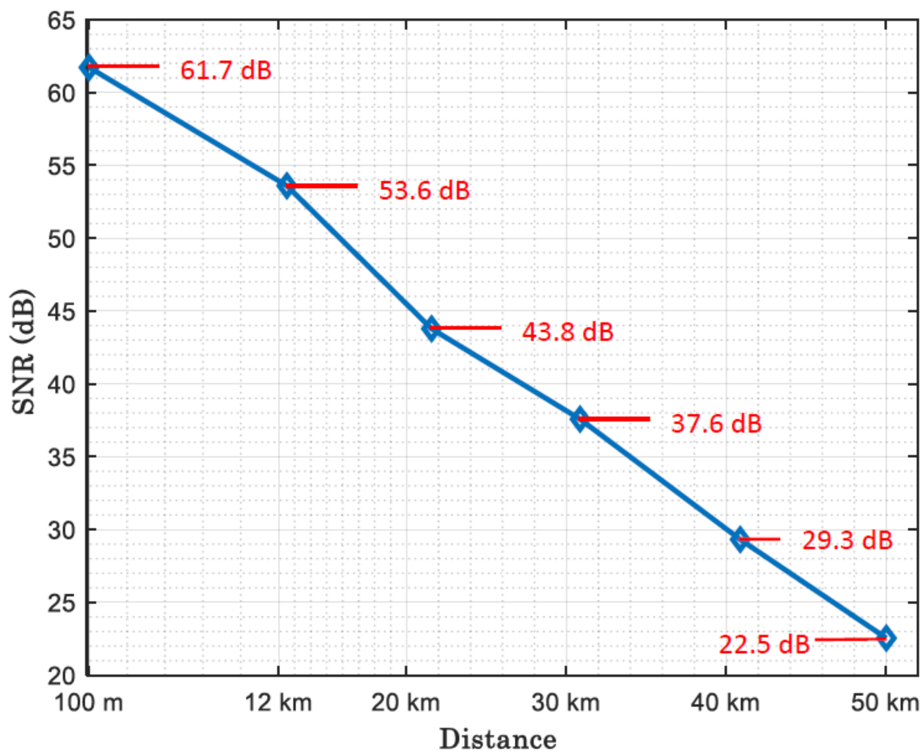

Figure 5.10: Mean SNR values in 6 different regions. It shows a linear decrease in dB scale and the system has a performance of 22.5 dB at 50 km.

Chapter 6

Conclusion and Future Work

Phase-sensitive optical time domain reflectometer ($\phi-$OTDR) based distributed acoustic sensor (DAS) has found a widespread application in many areas. Its ability of continuous and large-area sensing and monitoring the variations makes the DAS a high-demand and sought-after technology especially in health monitoring and security of large structures such as oil and gas pipelines, bridges, railways, dams and other military and civil constructions.

In this thesis, we have focused on $\phi-$OTDR based direct detection DAS systems. We have firstly reviewed the fundamentals of optical fibers, and then investigated the theory of Rayleigh scattering in optical fibers followed by the principles of OTDR and $\phi-$OTDR systems.

We have established the set-up in laboratory and explained the building components of the system. Before the system level investigation, we have tested and characterized the important parameters of the key components including laser, EDFA, AOM, optical bandpass filters and photodetector. We have preferred a narrow linewidth and low frequency drift light source for a better performance.

We have then conducted the laboratory tests and analyzed the fiber stretcher (piezoelectric transducer - PZT) induced phase shifts at different locations of the test fibers. We have first constructed the test set-ups and determined the system parameters, and then tested the ability of vibration detection of our system, varying the PZT signal types, amplitudes, distances. Since the peak values of continuous PZT vibration signals were varying in time due to the randomness of the system and fading phenomena, we have measured SNR values within certain time windows and proposed mean SNR as a new performance metric. We have also experimentally analyzed the non-linearity and power transfer to the harmonics for large values of PZT voltages using the proposed mean SNR parameter.

Furthermore, we have studied the photon statistics of Rayleigh backscattered signal in the presence of amplified spontaneous emission (ASE) noise to have a better understanding of the background signal. Our theoretical modeling and experimental results have demonstrated that the distribution of the Rayleigh backscattered signal intensity in a direct-detection DAS system does not remain negative exponential in the presence of optical preamplifiers. This is attributed to the Gaussian components added by ASE noise of the preamplifier, mean and standard deviation depending on the distance along the fiber and the bandwidth of the optical band-pass filters placed after the preamplifier. We have shown that Ex-Gaussian pdf is useful and effective to characterize the distributions which include the effect of ASE noise. We have also demonstrated that the mean SNR of the system increases with better filtering of ASE noise.

After laboratory tests, we have performed field tests of the system where the events of digging, walking and motor vibration were investigated. We have located the positions of events at different distances of 50 km-long fiber and observed the effects of activities in the field. We have applied some signal processing algorithms to increase the visibility of the peaks created by digging strikes and walking steps. The peaks were clearly visible along the 50 km-long fiber after optimizing the system parameters and applying the algorithm. We have finally measured the intensities of motor vibration signal over the monitored regions and calculated their SNRs within certain time windows (33.75 sec). The resulting SNR values were used to generate corresponding histograms in 6 different locations from 100 m to 50 km along the fiber. We have calculated mean SNR values and shown over these histograms and shown linear decrease with the distance as expected.

The future work of the thesis has different paths. One of them is the theoretical investigation of the SNR distribution plots. It would help us to analyze and simulate the system performance much better than our knowledge we have now. Another is expanding the model of the ASE noise included Rayleigh backscattered signal presented in Section 4.3. Calculations of the exact fitting parameters and numerical simulations can be performed to support experimental data. The other future works are mainly in the experimental setup side of the thesis. Certain methods can be implemented to increase the system performance and statistical parameters of the modified system can be calculated to quantify the amount of performance improvement.

Bibliography

[1] A. H. Hartog, *An introduction to distributed optical fibre sensors*. CRC Press, 2017.

[2] M. Barnoski and S. Jensen, "Fiber waveguides: a novel technique for investigating attenuation characteristics," *Applied optics*, vol. 15, no. 9, pp. 2112–2115, 1976.

[3] M. Barnoski, M. Rourke, S. Jensen, and R. Melville, "Optical time domain reflectometer," *Applied optics*, vol. 16, no. 9, pp. 2375–2379, 1977.

[4] A. Hartog and D. Payne, "A fibre-optic temperature-distribution sensor," 1982.

[5] T. Horiguchi, T. Kurashima, and M. Tateda, "A technique to measure distributed strain in optical fibers," *IEEE photonics technology letters*, vol. 2, no. 5, pp. 352–354, 1990.

[6] T. Kurashima, T. Horiguchi, and M. Tateda, "Distributed-temperature sensing using stimulated brillouin scattering in optical silica fibers," *Optics letters*, vol. 15, no. 18, pp. 1038–1040, 1990.

[7] M. Tateda, T. Horiguchi, T. Kurashima, and K. Ishihara, "First measurement of strain distribution along field-installed optical fibers using brillouin spectroscopy," *Journal of Lightwave Technology*, vol. 8, no. 9, pp. 1269–1272, 1990.

[8] K. Shimizu, T. Horiguchi, Y. Koyamada, and T. Kurashima, "Coherent self-heterodyne detection of spontaneously brillouin-scattered light waves in a single-mode fiber," *Optics letters*, vol. 18, no. 3, pp. 185–187, 1993.

[9] H. F. Taylor and C. E. Lee, "Apparatus and method for fiber optic intrusion sensing," Mar. 16 1993. US Patent 5,194,847.

[10] R. Juškaitis, A. Mamedov, V. Potapov, and S. Shatalin, "Distributed interferometric fiber sensor system," *Optics letters*, vol. 17, no. 22, pp. 1623–1625, 1992.

[11] R. Juškaitis, A. Mamedov, V. Potapov, and S. Shatalin, "Interferometry with rayleigh backscattering in a single-mode optical fiber," *Optics letters*, vol. 19, no. 3, pp. 225–227, 1994.

[12] Z. Qin, *Distributed optical fiber vibration sensor based on Rayleigh backscattering*. PhD thesis, Université d'Ottawa/University of Ottawa, 2013.

[13] Y. Lu, T. Zhu, L. Chen, and X. Bao, "Distributed vibration sensor based on coherent detection of phase-otdr," *Journal of lightwave Technology*, vol. 28, no. 22, pp. 3243–3249, 2010.

[14] Z. Wang, L. Zhang, S. Wang, N. Xue, F. Peng, M. Fan, W. Sun, X. Qian, J. Rao, and Y. Rao, "Coherent ϕ-otdr based on i/q demodulation and homodyne detection," *Optics express*, vol. 24, no. 2, pp. 853–858, 2016.

[15] H. Liu, F. Pang, L. Lv, X. Mei, Y. Song, J. Chen, and T. Wang, "True phase measurement of distributed vibration sensors based on heterodyne ϕ-otdr," *IEEE Photonics Journal*, vol. 10, no. 1, pp. 1–9, 2018.

[16] Z. Wang, J. Zeng, J. Li, M. Fan, H. Wu, F. Peng, L. Zhang, Y. Zhou, and Y. Rao, "Ultra-long phase-sensitive otdr with hybrid distributed amplification," *Optics letters*, vol. 39, no. 20, pp. 5866–5869, 2014.

[17] H. F. Martins, S. Martín-López, P. Corredera, M. L. Filograno, O. Frazao, and M. Gonzalez-Herráez, "Phase-sensitive optical time domain reflectometer assisted by first-order raman amplification for distributed vibration sensing over¿ 100 km," *Journal of Lightwave Technology*, vol. 32, no. 8, pp. 1510–1518, 2014.

[18] G. Fang, T. Xu, S. Feng, and F. Li, "Phase-sensitive optical time domain reflectometer based on phase-generated carrier algorithm," *Journal of Lightwave Technology*, vol. 33, no. 13, pp. 2811–2816, 2015.

[19] A. Masoudi, M. Belal, and T. Newson, "A distributed optical fibre dynamic strain sensor based on phase-otdr," *Measurement Science and Technology*, vol. 24, no. 8, p. 085204, 2013.

[20] D. Chen, Q. Liu, X. Fan, and Z. He, "Distributed fiber-optic acoustic sensor with enhanced response bandwidth and high signal-to-noise ratio," *Journal of Lightwave Technology*, vol. 35, no. 10, pp. 2037–2043, 2017.

[21] Z. Pan, K. Liang, Q. Ye, H. Cai, R. Qu, and Z. Fang, "Phase-sensitive otdr system based on digital coherent detection," in *Asia Communications and Photonics Conference and Exhibition*, p. 83110S, Optical Society of America, 2011.

[22] Z. Qin, T. Zhu, L. Chen, and X. Bao, "High sensitivity distributed vibration sensor based on polarization-maintaining configurations of phase-otdr," *IEEE Photon. Technol. Lett.*, vol. 23, no. 15, pp. 1091–1093, 2011.

[23] K. Shimizu, T. Horiguchi, and Y. Koyamada, "Characteristics and reduction of coherent fading noise in rayleigh backscattering measurement for optical fibers and components," *Journal of Lightwave Technology*, vol. 10, no. 7, pp. 982–987, 1992.

[24] Z. Pan, K. Liang, J. Zhou, Q. Ye, H. Cai, and R. Qu, "Interference-fading-free phase-demodulated otdr system," in *OFS2012 22nd International Conference on Optical Fiber Sensors*, vol. 8421, p. 842129, International Society for Optics and Photonics, 2012.

[25] Y. Shi, H. Feng, and Z. Zeng, "A long distance phase-sensitive optical time domain reflectometer with simple structure and high locating accuracy," *Sensors*, vol. 15, no. 9, pp. 21957–21970, 2015.

[26] M. Ren, P. Lu, L. Chen, and X. Bao, "Theoretical and experimental analysis of $\phi-$otdr based on polarization diversity detection," *IEEE Photonics Technology Letters*, vol. 28, no. 6, pp. 697–700, 2016.

[27] Y. Zhang, Y. Xu, Y. Shan, Z. Sun, F. Zhu, and X. Zhang, "Polarization dependence of phase-sensitive optical time-domain reflectometry and its suppression method based on orthogonal-state of polarization pulse pair," *Optical Engineering*, vol. 55, no. 7, p. 074109, 2016.

[28] H. Gabai and A. Eyal, "Snr characterization in distributed acoustic sensing," in *Sixth European Workshop on Optical Fibre Sensors*, vol. 9916, p. 99162W, International Society for Optics and Photonics, 2016.

[29] A. Eyal, H. Gabai, and I. Shpatz, "Distributed acoustic sensing: how to make the best out of the rayleigh-backscattered energy?," in *Optical Fiber Sensors Conference (OFS), 2017 25th*, pp. 1–4, IEEE, 2017.

[30] "Fs.com - the capable optical fiber cable." https://www.fs.com/network-communication-cables-that-power-your-internet-aid-393.html. Accessed: 2018-08-01.

[31] R. Paschotta, "Field guide to optical fiber technology," SPIE, 2010.

[32] J. Zubia and J. Arrue, "Plastic optical fibers: An introduction to their technological processes and applications," *Optical fiber technology*, vol. 7, no. 2, pp. 101–140, 2001.

[33] J. Knight, T. Birks, P. S. J. Russell, and D. Atkin, "All-silica single-mode optical fiber with photonic crystal cladding," *Optics letters*, vol. 21, no. 19, pp. 1547–1549, 1996.

[34] P. Russell, "Photonic crystal fibers," *science*, vol. 299, no. 5605, pp. 358–362, 2003.

[35] J. M. Senior and M. Y. Jamro, *Optical fiber communications: principles and practice*. Pearson Education, 2009.

[36] G. P. Agrawal, *Lightwave technology: telecommunication systems*. John Wiley & Sons, 2005.

[37] J. L. Santos and F. Farahi, *Handbook of optical sensors*. Crc Press, 2014.

[38] R. Ellis, "Explanation of reflection features in optical fiber as sometimes observed in otdr measurement traces," *Corning White Paper*, 2007.

[39] D. Dennis, "Fiber optic test and measurement," *Print Hall, New Jersey*, 1998.

[40] A. K. Wojcik, *Signal statistics of phase dependent optical time domain reflectometry*. PhD thesis, Texas A&M University, 2007.

[41] "Anritsu, understanding otdrs." https://rossfibersolutions.com/fiber-optic-pdfs/Anritsu-understanding-otdrs.pdf. Accessed: 2010-08-01.

[42] M. Ren, *Distributed Optical Fiber Vibration Sensor Based on Phase-Sensitive Optical Time Domain Reflectometry*. PhD thesis, Université d'Ottawa/University of Ottawa, 2016.

[43] K. N. Choi and H. F. Taylor, "Spectrally stable er-fiber laser for application in phase-sensitive optical time-domain reflectometry," *IEEE Photonics technology letters*, vol. 15, no. 3, pp. 386–388, 2003.

[44] J. C. Juarez, E. W. Maier, K. N. Choi, and H. F. Taylor, "Distributed fiber-optic intrusion sensor system," *Journal of lightwave technology*, vol. 23, no. 6, pp. 2081–2087, 2005.

[45] X. Liu, B. Jin, Q. Bai, Y. Wang, D. Wang, and Y. Wang, "Distributed fiber-optic sensors for vibration detection," *Sensors*, vol. 16, no. 8, p. 1164, 2016.

[46] X. Bao and L. Chen, "Recent progress in distributed fiber optic sensors," *Sensors*, vol. 12, no. 7, pp. 8601–8639, 2012.

[47] H. F. Martins, S. Martin-Lopez, P. Corredera, M. L. Filograno, O. Frazão, and M. González-Herráez, "Coherent noise reduction in high visibility phase-sensitive optical time domain reflectometer for distributed sensing of ultrasonic waves," *Journal of Lightwave Technology*, vol. 31, no. 23, pp. 3631–3637, 2013.

[48] "Itu - g.694.1 : Spectral grids for wdm applications: Dwdm frequency grid." http://www.itu.int/rec/T-REC-G.694.1-201202-I/en. Accessed: 2010-08-01.

[49] L. Shi, T. Zhu, Q. He, and S. Huang, "Effect of laser linewidth on phase-otdr based distributed vibration sensing regime," in *23rd International Conference on Optical Fibre Sensors*, vol. 9157, p. 91576H, International Society for Optics and Photonics, 2014.

[50] A. Zhirnov, A. Fedorov, K. Stepanov, E. Nesterov, V. Karasik, C. Svelto, and A. Pnev, "Effects of laser frequency drift in phase-sensitive optical time-domain reflectometry fiber sensors," *arXiv preprint arXiv:1604.08854*, 2016.

[51] X. Zhong, C. Zhang, L. Li, S. Liang, Q. Li, Q. Lü, X. Ding, and Q. Cao, "Influences of laser source on phase-sensitivity optical time-domain reflectometer-based distributed intrusion sensor," *Applied optics*, vol. 53, no. 21, pp. 4645–4650, 2014.

[52] "Acousto-optic modulation." http://www.isomet.com/App-Manualpdf/AO20Modulation.pdf. Accessed: 2010-08-01.

[53] C. Baker, B. Vanus, M. Wuilpart, L. Chen, and X. Bao, "Enhancement of optical pulse extinction-ratio using the nonlinear kerr effect for phase-otdr," *Optics express*, vol. 24, no. 17, pp. 19424–19434, 2016.

[54] L. B. Liokumovich, N. A. Ushakov, O. I. Kotov, M. A. Bisyarin, and A. H. Hartog, "Fundamentals of optical fiber sensing schemes based on coherent optical time domain reflectometry: Signal model under static fiber conditions," *Journal of Lightwave Technology*, vol. 33, no. 17, pp. 3660–3671, 2015.

[55] X. He, S. Xie, F. Liu, S. Cao, L. Gu, X. Zheng, and M. Zhang, "Multi-event waveform-retrieved distributed optical fiber acoustic sensor using dual-pulse heterodyne phase-sensitive otdr," *Optics letters*, vol. 42, no. 3, pp. 442–445, 2017.

[56] G. H. Ames and W. R. Donat, "Fading statistics in rayleigh interferometric fiber sensors," in *23rd International Conference on Optical Fibre Sensors*, vol. 9157, p. 915767, International Society for Optics and Photonics, 2014.

[57] G. R. Osche, "Optical detection theory for laser applications," *Optical Detection Theory for Laser Applications, by Gregory R. Osche, pp. 424. ISBN 0-471-22411-1. Wiley-VCH, July 2002.*, p. 424, 2002.

[58] J. W. Goodman, "Statistical properties of laser speckle patterns," in *Laser speckle and related phenomena*, pp. 9–75, Springer, 1975.

[59] P. Healey, "Statistics of rayleigh backscatter from a single-mode fiber," *IEEE transactions on communications*, vol. 35, no. 2, pp. 210–214, 1987.

[60] R. Steele, G. Walker, and N. Walker, "Sensitivity of optically preamplified receivers with optical filtering," *IEEE Photonics Technology Letters*, vol. 3, no. 6, pp. 545–547, 1991.

[61] S. Donati and G. Giuliani, "Noise in an optical amplifier: Formulation of a new semiclassical model," *IEEE journal of quantum electronics*, vol. 33, no. 9, pp. 1481–1488, 1997.